https://doi.org/10.5194/egusphere-2025-4819
Preprint. Discussion started: 9 October 2025

Global identification of dominant ice-particle growth in cirrus clouds using EarthCARE satellite observations

Tatsuya Seiki[1], Hiroaki Horie[2], Yuichiro Hagihara[2], Shunsuke Aoki[3], Akira T. Noda[1]

[1] Japan Agency for Marine-Earth Science and Technology, Yokohama, Kanagawa, 236-0001, Japan
[2] National Institute of Information and Communications Technology, Koganei, Tokyo, 184-8795, Japan
[3] Earth Observation Research Center, Japan Aerospace Exploration Agency, Tsukuba, Ibaraki, 305-8505, Japan

Correspondence to: Tatsuya Seiki (tseiki@jamstec.go.jp)

Abstract. This study applies an ice-particle growth identification method to global observations obtained from the EarthCARE satellite. The method uses a joint probability density function of the equivalent radar reflectivity factor (Z_e) and Doppler velocity (v_d) on a common logarithmic scale (Z_e–$\log_{10}v_d$ diagram), where the ratio of changes in Z_e to changes in $\log_{10}v_d$ —referred to as the slope—serves as a quantitative indicator of dominant cloud microphysical processes. The analysis investigates the impact of random noise in Doppler velocity, which is a critical issue in EarthCARE products. In particular, three major error sources are addressed: observation window mode, along-track integration length, and bias correction related to antenna thermal distortion. These factors are found to significantly affect the derivation of slope values. To minimize the influence of noise, a representative slope is defined by calculating the median Doppler velocity in each Z_e bin before applying the $\log_{10}$ transformation. Using this revised method, EarthCARE's global observations reveal a systematic increase in the representative slope with atmospheric temperature across all latitude bands. While regional variations in slope are generally small, they nonetheless reflect distinctive microphysical characteristics specific to each region. These findings demonstrate that the EarthCARE satellite can be used to globally monitor cirrus cloud growth processes and offer a quantitative metric for evaluating the performance of climate models in representing cloud microphysics.

Short Summary. How ice particles grow in extremely cold conditions remains poorly understood due to limited observations. This study develops a new method to identify dominant ice-particle growth from radar reflectivity and Doppler velocity. It reveals, for the first time, that key growth processes vary not only with temperature but also by region. These findings highlight EarthCARE's value for monitoring clouds and improving climate model representation.

1 Introduction

The EarthCARE satellite is equipped with four sensors to comprehensively understand the hydrosphere under the strong influences of clouds, aerosols, and radiation. In particular, the spaceborne W-band cloud profiling radar with Doppler capability (CPR) is the most distinctive feature of the satellite (Kollias et al., 2014). In general, cloud particles grow within a

https://doi.org/10.5194/egusphere-2025-4819
Preprint. Discussion started: 9 October 2025

moist ascending air parcel and eventually form precipitation once they become sufficiently heavy. Thus, observations of vertical air motion are essential for understanding the mechanism of particle growth.

The EarthCARE satellite was scheduled for launch in 2018 (Illingworth et al., 2015) and was finally launched on 28 May 2024. During this preparation period, analysis methods for CPR have been developed. For instance, satellite signal simulators (Hashino et al., 2013; 2016; 2025; Reverdy et al., 2015; Voors et al., 2017) has been elaborated to examine CPR signals before its launch. The simulators are capable to generate the equivalent radar reflectivity factor (Z_e) and Doppler velocity (v_d) based on atmospheric simulations. The initial attempt of model evaluation was to compare the vertical distribution of v_d, as had been done with the equivalent radar reflectivity factor Z_e using CloudSat satellite observations (e.g., Hashino et al., 2013). Through the early evaluation of atmospheric models using in-situ observations (e.g., Roh et al., 2024), Doppler velocity observations have been shown to be sensitive to distinguish different cloud microphysics schemes. Subsequently, new metrics to directly evaluate cloud microphysical processes using Doppler radar are desired.

Recently, a novel analysis method that jointly utilizes simultaneous observations of Z_e and v_d was proposed based on in-situ ground-based radar observations prior to the launch of the EarthCARE satellite (Seiki et al., 2025). This analysis enables us to estimate key cloud microphysical processes in cirrus clouds with a quantitative index. With the release of the EarthCARE Level 2 product on 17 May 2025, this study finally applies this new analysis method to EarthCARE observations. However, according to the Algorithm Theoretical Basis Document (ATBD) for the Level 2 product edited by the Japan Aerospace Exploration Agency (JAXA), some practical issues need to be addressed in its application. After the launch, the EarthCARE Level 1 products, which are the sources of the Level 2 product, have been calibrated and validated. Subsequently, two major error sources were estimated as expected in the pre-launch analyses and an additional error source due to the harsh space environment was identified. This study examines the impact of these error sources to the analysis results to confirm the usefulness of the analysis method with the satellite observations.

The analysis method is briefly described in Section 2. Subsequently, the error sources and expectation of the influences of the errors to the method are described in Section 3. In Section4, the revised version of the analysis method is then proposed to address the issues found in Section 3. Section 5 shows the results of the global analysis using EarthCARE satellite observations. Section 6 discusses issues related to the analysis of W-band observations. Finally, findings are summarized in Section 7.

2 Analysis Method

2.1 Analysis using Z_e–$\log_{10}v_d$ diagram

The novel analysis method using the Z_e–$\log_{10}v_d$ diagram proposed by Seiki et al. (2025) is briefly documented here. Assuming that the mass concentration M [kg m^{-3}], representing the average mass concentration within a radar range bin, follows a power law of the mean particle diameter $\bar{D}$ [m] as $M \propto \bar{D}^b$ ($2 \leq b \leq 3$), the equivalent radar reflectivity factor Z_e [dBZ] in Rayleigh scattering regions is represented as follows:

https://doi.org/10.5194/egusphere-2025-4819
Preprint. Discussion started: 9 October 2025

$$Z_e = 10\log_{10} M + (60 - 10b)10\log_{10} \bar{D} + c. \quad (1)$$

where c is a coefficient related to unit conversion and the weighting used in the integration over the particle size distribution. Thus, a change in Z_e attributes to a change in M and a change in $\bar{D}$ as follows:

$$\Delta Z_e = 10\log_{10} e \frac{\Delta M}{M} + (60 - 10b)\log_{10} e \frac{\Delta \bar{D}}{\bar{D}}. \quad (2)$$

Similarly, a change in Doppler velocity v_d is expressed in a common logarithmic scale as follows:

$$\Delta \log_{10}(v_d) = \log_{10} e\, \beta \frac{\Delta \bar{D}}{\bar{D}}, \quad (3)$$

with two simplifications involving the ice terminal velocity v_t:

$$v_t = \alpha \bar{D}^{\beta}, (0.5 \leq \beta \leq 2) \quad (4)$$

$$v_d \sim v_t. \quad (5)$$

Thus, a change in v_d also attributes to a change in $\bar{D}$ under an assumption that atmospheric vertical motion is sufficiently small compared to v_t.

By dividing Eq. (2) by Eq. (3), the relationship between Z_e and v_d can finally be directly explained by microphysical properties as follows:

$$\frac{\Delta Z_e}{\Delta \log_{10} v_d} = \frac{10}{\beta}\frac{\bar{D}}{M}\frac{\Delta M}{\Delta \bar{D}} + \frac{60-10b}{\beta}. \quad (6)$$

Based on Eq. (6), the slope on the two-dimensional parameter space of Z_e and $\log_{10} v_d$ represents the variation in the mass concentration with respect to the mean particle size that is the sensitive to microphysical processes.

When particles size becomes sufficiently large to be in Mie scattering regions, in which size parameter is larger than 1 ($D > 10^{-3}$ m for CPR), radar reflectivity factor is proportional to square of particle size. Eq. (1) and subsequently Eq. (6) need to be modified as follows:

$$\frac{\Delta Z_e}{\Delta \log_{10} v_d} = \frac{10}{\beta}\frac{\bar{D}}{M}\frac{\Delta M}{\Delta \bar{D}} + \frac{20-10b}{\beta} \sim \frac{10}{\beta}\frac{\bar{D}}{M}\frac{\Delta M}{\Delta \bar{D}}. \quad (7)$$

In such a case, $b \sim 2$ gives a good approximation since large ice particles are likely to grow two-dimensionally (e.g., Mitchell, 1996; Westbrook et al., 2004). Therefore, the second term in the right-hand side of Eq. (7) is negligible. Comparing Eq. (7) to Eq. (6), the slope is expected to be smaller at larger v_d ranges.

This method can be utilized for non-convective cloud systems since Doppler velocity should be positive in a logarithmic scale (Eq. 3). In such cloud systems, quasi-stationary downdraft exists associated with snowfall drag. However, influences of such vertically uniform air-motion to this analysis, in which the simplification of Eq. (5) is applied, can be mostly cancelled by differentiate Doppler velocity as Eq. (3).

To characterize key cloud microphysical processes in cloud layers, a joint probability density function (JPDF) of Z_e and $\log_{10} v_d$ is made in the cloud layers, and subsequently, the first principal component in the JPDF indicates the representative sensitivity in the cloud layers (Eqs. 6-7). Hereafter, the JPDF is referred to as the Z_e–$\log_{10} v_d$ diagram.

https://doi.org/10.5194/egusphere-2025-4819
Preprint. Discussion started: 9 October 2025

2.2 Reference analysis using in-situ observations

In prior to the analysis using the EarthCARE satellite observations, the principal component analysis (PCA) using in-situ ground radar observations are shown as the reference. This study analyzed the same in-situ observations as Seiki et al. (2025), who utilized annual observations from January to December 2022 derived from the High-sensitivity Ground-based Super Polarimetric Ice-crystal Detection and Explication Radar (HG-SPIDER; Horie et al., 2000) located in Koganei City, Japan (35.7°N, 139.5°E). Cloudy pixels were identified using a radar reflectivity threshold greater than -35 dBZ based on the EarthCARE Level 2 ATBD although HG-SPIDER has greater sensitivity to cloud layers than CPR (Horie et al., 2000).

In this study, ice particles that grow while falling are sampled using thresholds for the vertical gradient of Z_e and v_d as follows:

$$\frac{\partial Z_e}{\partial T_a} > \left(\frac{\partial Z_e}{\partial T_a}\right)_{min}, \tag{8}$$

$$\frac{\partial \log_{10} v_d}{\partial T_a} > \left(\frac{\partial \log_{10} v_d}{\partial T_a}\right)_{min}, \tag{9}$$

$$v_d > 0. \tag{10}$$

The thresholds, $\left(\frac{\partial Z_e}{\partial T_a}\right)_{min} = 0.01$ [dBZ K^{-1}] and $\frac{\partial \log_{10} v_d}{\partial T_a} = 0.001$ [K^{-1}], were chosen based on in-situ ground radar observations (Seiki et al., 2025). In addition, atmospheric temperature inversion layers were excluded from the analysis.

Figure 1 shows the Z_e–$\log_{10} v_d$ diagram at various atmospheric temperature ranges in the upper troposphere. In general, the mean Z_e increases with increasing atmospheric temperatures as is expected in the sampling method (Eqs. 8-9). In addition, an increase in the slope is also found with increasing atmospheric temperatures. This indicates the transition of the microphysical sensitivity from the cloud top toward cloud base, which is strongly constrained by atmospheric temperatures.

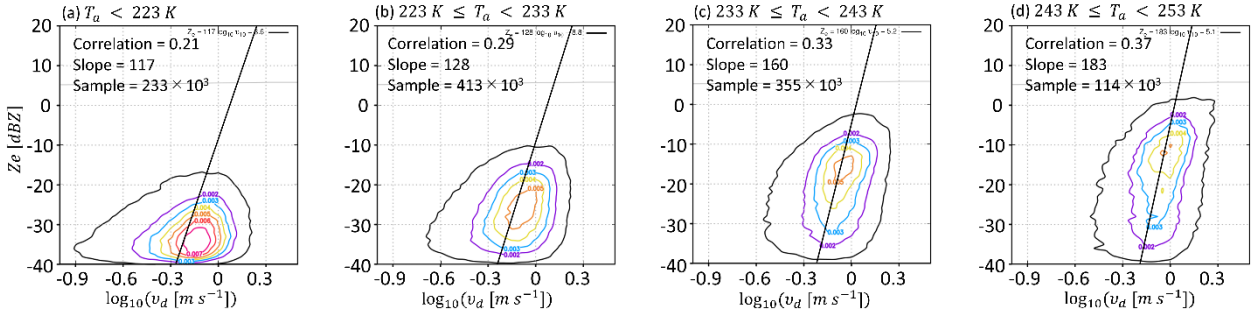

Figure 1: The Z_e–$\log_{10} v_d$ diagram with the representative slopes (black lines) derived from PCA of HG-SPIDER observations. Ice clouds were individually sampled separately across four atmospheric temperature ranges, each spanning 10 K. The representative slope, correlation coefficient, and sample size are indicated. The black contour encloses approximately 90% of the samples, and principal component analysis was conducted within this region to minimize the influence of outliers. Here, the joint PDF was converted into probability mass (i.e., the probability within each bin) by multiplying by the bin area ($\Delta x \cdot \Delta y$), enabling resolution-independent interpretation.

https://doi.org/10.5194/egusphere-2025-4819
Preprint. Discussion started: 9 October 2025

Based on Seiki et al. (2025), variation in the slope is explained aided with microphysical theory. For instance, in aggregation, M does not change while $\overline{D}$ increases. Thus, the first term in the right-hand side of Eq. (6) is negligible, and consequently, the slope is estimated as a fixed value as:

$$\frac{\Delta Z_e}{\Delta \log_{10} v_d} \sim \frac{60-10b}{\beta}. \quad (11)$$

In vapor deposition, an increase in $\overline{D}$ attributes to only an increase in M since the number concentration N does not change. Thus, the mass-diameter relationship ($M \propto \overline{D}^b$) determines the microphysical sensitivity.

Given $M = a\overline{D}^b$ with a coefficient a,

$$\frac{\overline{D}}{M}\frac{\Delta M}{\Delta \overline{D}} = b. \quad (12)$$

Thus, the slope is readily obtained as a constant as follows:

$$\frac{\Delta Z_e}{\Delta \log_{10} v_d} = \frac{10b}{\beta} + \frac{60-10b}{\beta} = \frac{60}{\beta}. \quad (13)$$

In the upper troposphere, cloud microphysical processes of ice nucleation, aggregation, vapor deposition, sublimation, and gravitational sedimentation dominate. With a focus on cloud systems in that particles grow downward as defined by Eqs. (8-10), ice nucleation and sublimation do not act a key role, and hence, the microphysical balance among aggregation, vapor deposition, and gravitational sedimentation can be estimated. Based on Eqs. (6), (11), and (13), relatively steeper slope values exhibit in depositional growth mode compared aggregational growth mode. In this manner, the increase in the slope toward cloud base (Fig. 1) is interpreted as the dominance of vapor deposition toward cloud base, related to abundant water vapor mass concentration under warmer atmospheric conditions.

For the seasonal matching to the EarthCARE Level 2 products, the Z_e–$\log_{10}v_d$ diagrams obtained from January to March are also shown in Figure 2. The slope values and correlation coefficients are found to strongly depend on sample number. In particular, correlation coefficients between Z_e and $\log_{10}v_d$ are small at atmospheric temperatures colder than 233 K. Correspondingly, slope values in the temperature ranges are not reliable due to insufficient sample size.

The sufficient sample sizes were evaluated by varying the analysis period. Figure 3 shows the changes in sample sizes and correlation coefficients over time. In general, required sample size differs depending on the temperature range, and the statistical behaviors of Z_e and $\log_{10}v_d$ becomes more unstable at colder temperatures. An analysis period of at least nine months is necessary to establish a reliable relationship between Z_e and $\log_{10}v_d$ for all temperature ranges. Specifically, the required sample sizes are approximately 200,000 for $T_a < 223$ K, 350,000 for 223 K $\leq T_a <$ 233 K, 300,000 for 233 K $\leq T_a <$ 243 K, and 100,000 for 243K $\leq T_a <$ 253K. Thus, in the EarthCARE analysis presented later, this study prioritizes matching sample sizes over seasonal consistency.

The differences in the required sample sizes depending on the temperature range indicate that vertical air motion is not negligible near the cloud top of thin cirrus clouds. It is known that strong vertical wind shear and radiative heating or cooling in a thin cirrus layer induce instability in the cirrus layer; consequently, strong vertical air motion is frequently observed in

https://doi.org/10.5194/egusphere-2025-4819
Preprint. Discussion started: 9 October 2025

cirrus clouds near the tropopause (e.g., Yamazaki and Miura, 2021). Since such cloud systems have fine-scale dynamical structures, a larger sample size is required to smooth out the characteristics of individual cloud systems.

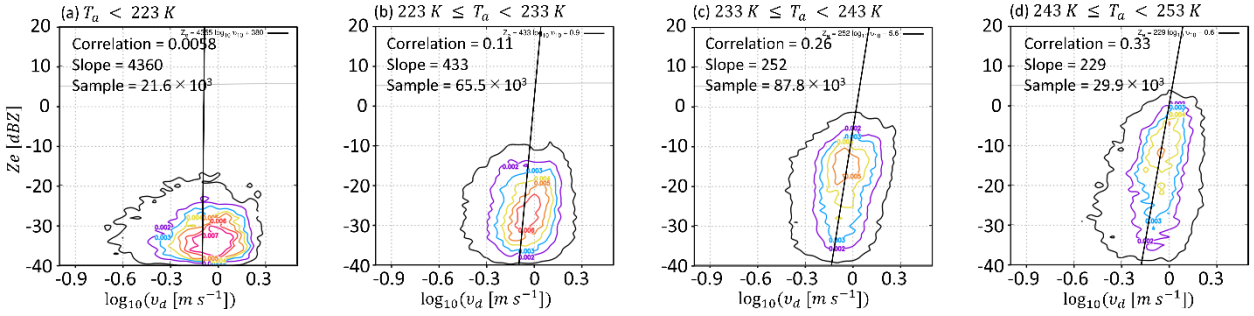

Figure 2. The same as Fig. 1 except for the analysis period from January to March 2022.

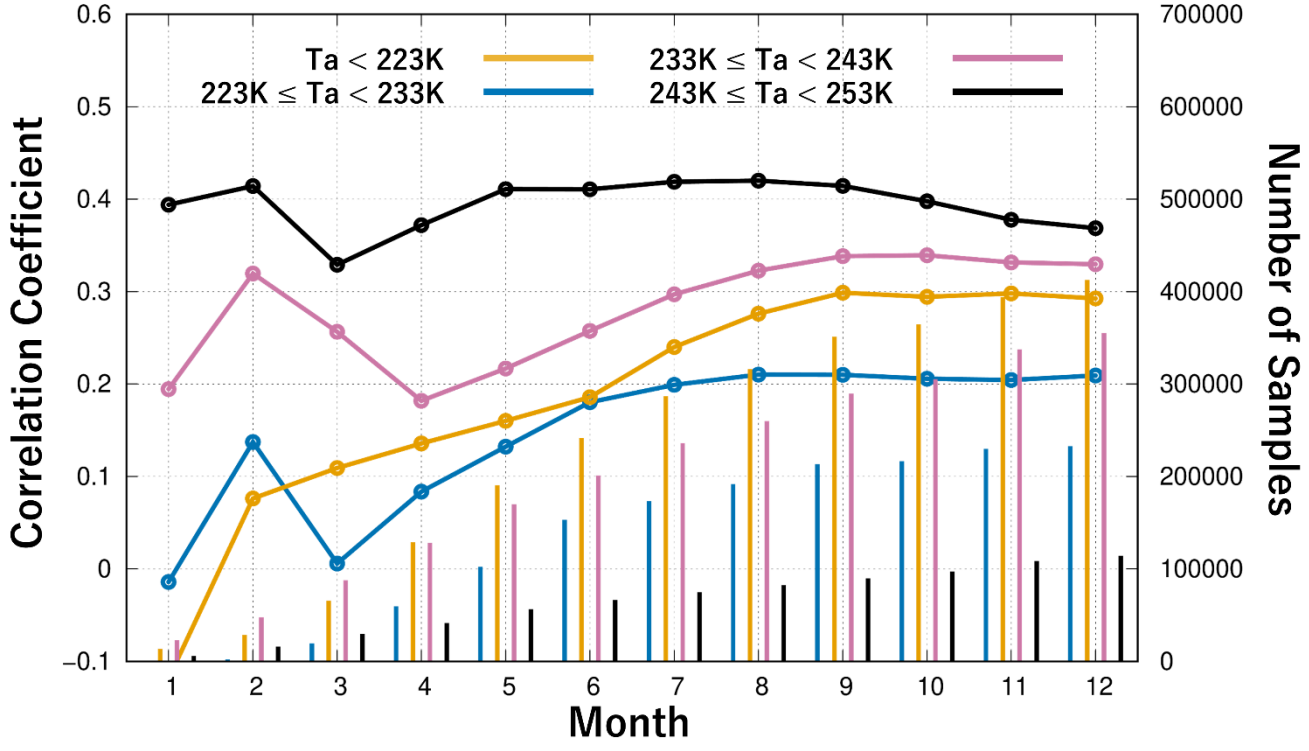

Figure 3. Evolution of the number of samples (color bars, right vertical axis) and correlation coefficients (color lines, left vertical axis) across the four temperature ranges with increasing months of data collection.

https://doi.org/10.5194/egusphere-2025-4819
Preprint. Discussion started: 9 October 2025

3 Known Error Sources and Their Impact on Analysis

This section describes three major known sources of error in the EarthCARE satellite observations. Other unknown error sources are not addressed in this study, as it is difficult to quantify their contribution to the analysis. Mirror echo signals are removed using the quality flag (f_{mirror}). Ground clutter in the integrated radar reflectivity (Z_{em}) is removed using the quality flag (f_{ze}) and an empirical threshold based on the distance from surface elevation. In addition, this study analyzes cloudy pixels with integrated radar reflectivity greater than -33 dBZ. These processing steps are described in detail in Appendix A.

The Level 2 and Level 1 products of CPR operated by JAXA (hereafter referred to as the JAXA L2 and L1 product) used in this study is summarized in Table 1. The L2A/CPR_ECO/vBa product is available for the period from January 13 to March 13, 2025 and the L1B/CPR_NOM/vCa product is available for the period from January 1 to March 13, 2025. The JAXA L1 product was used for examining the noise level in the L2 product.

Table 1. Variables from the JAXA L2 product (L2A/CPR_ECO/vBa) and L1 product (L1B/CPR_NOM/vCa) used in this study.

Variable name in HDF5 data	Symbol used in this manuscript
L2A/CPR_ECO_vBa	
unfolded_doppler_velocity_1km	$\upsilon_{dm,1km}$
unfolded_doppler_velocity_10km	$\upsilon_{dm,10km}$
unfolded_doppler_velocity_1km_bias_corr	$\upsilon_{dc,1km}$
unfolded_doppler_velocity_10km_bias_corr	$\upsilon_{dc,10km}$
integrated_radar_reflectivity_1km	$Z_{em,1km}$
integrated_radar_reflectivity_10km	$Z_{em,10km}$
surface_bin_number_1km	$nb_{sfc,1km}$
surface_bin_number_10km	$nb_{sfc,10km}$
surface_elevation	h_m
integrated_radar_reflectivity_flag_1km	f_{ze}
mirror_echo_flag_1km	f_{mirror}
L1B/CPR_NOM/vCa	
integrationNumberDoppler	M_p
rayHeaderLambda	λ
rayStatusPrf	PRF
rayQualityFlag	f_{ray}

3.1 Z_e–$\log_{10}\upsilon_d$ diagram from EarthCARE

Figure 4 shows the Z_e–$\log_{10}\upsilon_d$ diagram obtained using $Z_{em,1km}$ and $\upsilon_{dc,1km}$ in the JAXA L2 product in the same manner to the reference analysis (Section 2b). The diagram is calculated from 30°N to 60°N to obtain the sufficient samples for the analysis (cf. Fig. 3). Even without PCA, the dominant slope clearly deviates from that observed in ground-based Doppler radar data. Furthermore, no distinct mode is observed, and the overall distribution seems rather diffuse and poorly defined. In this study, we consider that the lack of a distinct mode in the joint PDF is primarily due to systematic errors associated with

https://doi.org/10.5194/egusphere-2025-4819
Preprint. Discussion started: 9 October 2025

Doppler velocity measurements from satellite observations. In the following subsection, we evaluate how major known errors affect the Z_e–$\log_{10}\upsilon_d$ analysis.

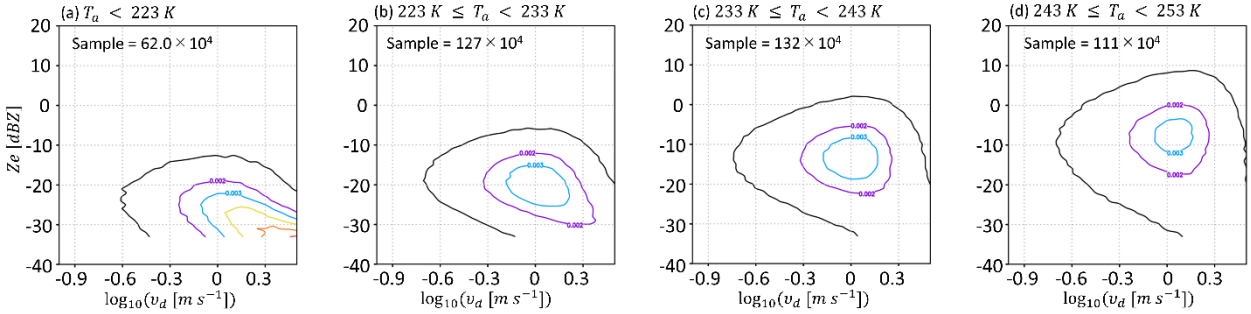

Figure 4. The Z_e–$\log_{10}\upsilon_d$ diagram at various atmospheric temperature ranges in the midlatitude calculated from the EarthCARE L2 product.

3.2 Integration length

In the Level 2 products, all physical quantities are provided in two versions, estimated separately using along-track integration lengths of 1 km and 10 km. Doppler velocity is measured using the pulse-pair method (Kobayashi et al., 2002; Hagihara et al., 2021), which evaluates the phase difference between two successive radar pulses (a pulse pair). In general, random noise in measured Doppler velocities decreases by averaging multiple pulse pairs; consequently, the accuracy of the Doppler velocity measurement is directly influenced by the pulse repetition frequency (PRF). Furthermore, residual random noise can be reduced by horizontally averaging measured Doppler velocities, even if the PRF is not increased (Hagihara et al., 2021; 2023). However, this post-processing also smooth outs fine-scale dynamical fluctuations. Ultimately, the mean Doppler velocity is obtained by integrating measured Doppler velocities over longer along-track distances, although the original integration length is approximately 500 m. It is important for users to carefully consider the choice of the integration length, as this choice uniformly affects the analysis results.

In this sub-section, the analysis error associated with the smoothing effect at a horizontal scale ten times coarser than the original is examined by temporally averaging the HG-SPIDER observations in the same manner as the CPR data (see Eqs. 6-10 in Hagihara et al., 2021). Considering a representative upper-tropospheric horizontal wind of 50 m s^{-1} over Japan during the analysis period, the original temporal integration time of one minute corresponds to a horizontal distance of approximately 3 km. Consequently, averaging 10 consecutive vertical profiles results in an effective horizontal integration length of 30 km, which is hereafter referred to as the "pseudo-30 km integration mode".

https://doi.org/10.5194/egusphere-2025-4819
Preprint. Discussion started: 9 October 2025

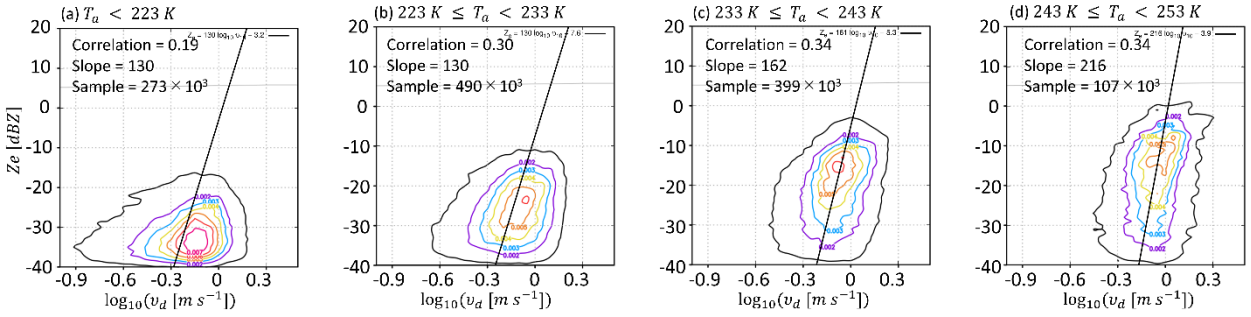

Figure 5. The same as Fig. 1 except for the post-processing. The HG-SPIDER observations were smoothed as the pseudo-30 km integration mode.

Figure 5 shows the Z_e–$\log_{10}\upsilon_d$ diagram obtained from the HG-SPIDER observations after applying the pseudo-30 km integration mode. In general, fine-scale dynamical fluctuations, which contribute to increasing the variance of $\log_{10}\upsilon_d$, are effectively suppressed by smoothing. As a result, the variances of both Z_e and $\log_{10}\upsilon_d$ slight decrease with temporal smoothing. However, the nonlinear relationship between Z_e and υ_d (Eqs. 1; 4-5), governed by cloud microphysical processes, becomes less clear due to smoothing. Thus, correlation coefficient slightly decreases by the temporal smoothing (Figs. 1; 5). In terms of evaluation of cloud microphysics, the slope can differ by at most 10% near the tropopause and 15% near the cloud bottom. These differences in slope due to smoothing are much smaller than the differences between HG-SPIDER observations and numerical simulation models (Seiki et al., 2025), and are therefore acceptable given the advantage of reducing random noise in CPR observations.

3.3 Observation window

In the observational configuration, two observation windows are defined based on tropopause height, which varies with latitude. A low mode is designed with an observation window ranging from -1 km to 16 km above sea level at latitudes north of 60°N or south of 60°S, while a high mode is designed with an observation window ranging from -1 km to 20 km above sea level at all other latitudes (Hagihara et al., 2021). Since a higher PRF is available in the low mode, radar signals in this mode are less affected by random error. For instance, when Z_e = -10 dBZ, the Doppler velocity has a random error of approximately 2 m s^{-1} in the 20 km mode, compared to approximately 1 m s^{-1} in the 16 km mode. Thus, the Level 1 products can effectively capture ice clouds near the tropopause using these two modes, but they are subject to different levels of random error across latitude bands due to differences in PRF settings.

The difference between observation window modes also affects the analysis results. Note that Z_e is less affected by random error due to the nature of radar reflectivity measurements, and therefore, does not differ significantly between the two observation window modes.

https://doi.org/10.5194/egusphere-2025-4819
Preprint. Discussion started: 9 October 2025

This study examines the contribution of random error to the PCA by artificially adding Gaussian noise, $\delta_{v,window}$, with a standard deviation of 1 m s^{-1} and zero mean, to the Doppler velocity measured by HG-SPIDER as follows:

$$v_{d,20km} = v_d + \delta_{v,window}, \quad (14)$$

This operation is hereafter referred to as the pseudo-20 km observation window mode.

In the PCA of the Z_e–log$_{10}v_d$ diagram, the sampling method that retains only the positive values of $v_{d,20km}$ (Eq. 10) distorts the probability density function (PDF) of random error. Figure 6 shows the difference between $v_{d,20km}$ and v_d before and after sampling. It is evident that the PDF of the sampled $v_{d,20km}$ values is positively biased, with a mean of approximately 0.76 m s^{-1} and a median of around 0.7 m s^{-1}.

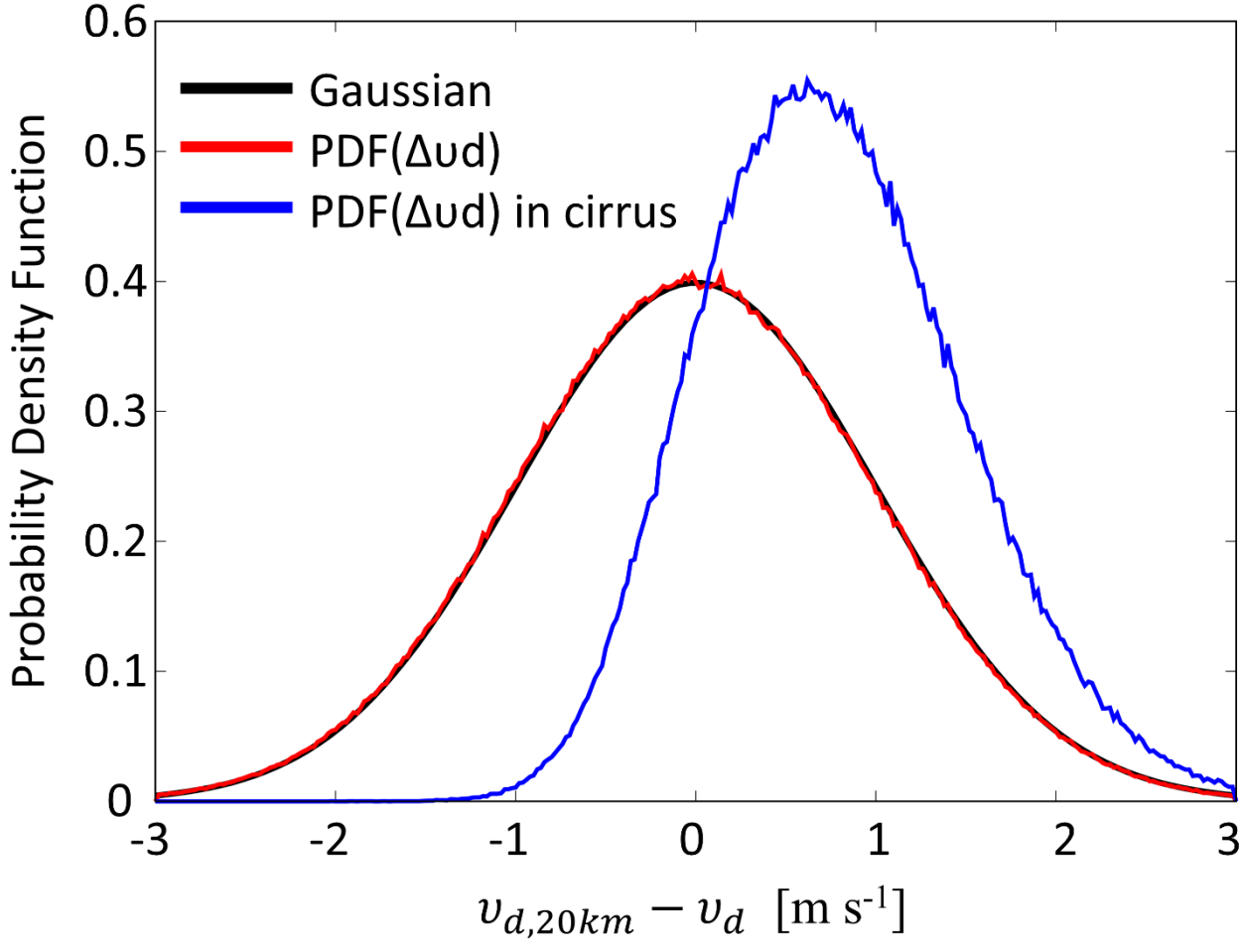

Figure 6. Probability density function (PDF) of the difference between $v_{d,20km}$ and v_d. The red line shows the PDF calculated for all cloudy layers, the blue for the targeted cirrus layers, and the black line shows a reference Gaussian distribution with a standard deviation of 1 m s^{-1} and no bias.

https://doi.org/10.5194/egusphere-2025-4819
Preprint. Discussion started: 9 October 2025

245

To assess the influence of this noise in the Z_e–$\log_{10}v_d$ diagram, the effect of the nonlinear logarithmic transformation is examined. Assuming small perturbations, the error propagates as:

$$\log_{10}(v_d + \delta_{v,window}) \sim \log_{10} v_d + \frac{1}{\ln(10) v_d}\delta_{v,window}. \quad (15)$$

This approximation shows that uncertainty in $\log_{10} v_d$ increases as v_d decreases, resulting in greater spread toward the left of
250 the diagram. Moreover, because negative v_d values are excluded, the lower tail of the $\log_{10}v_d$ distribution is truncated, introducing a right-skewed bias (Fig. 6). This right-skewed bias is particularly pronounced in regions with small Z_e, where v_d also tends to be small (cf. Fig. 3). As a result, the lower-left portion of the diagram becomes more dispersed, leading to a systematic steepening of the slope when the PCA is applied to the entire scatter distribution.

Figure 7 shows the Z_e–$\log_{10}v_d$ diagram obtained from the HG-SPIDER observations under the pseudo 20 km observation
255 window mode. The additional random noise systematically increases the mode value of v_d (Figs. 1; 7a-d), as mentioned above. In addition, the slope becomes steeper compared to the original Z_e-$\log_{10}v_d$ diagram as expected. Moreover, the correlation coefficient decreases, indicating the slope values become less reliable. Although the pseudo-30 km integration mode partially reduces the systematic bias in $\log_{10}v_d$, the improvement in the slope is quite limited (Figs. 1; 7e-h). These results indicate that the PCA is highly sensitive to large values of random error, particularly due to the nonlinear and
260 asymmetric nature of error propagation in the logarithmic domain.

The random error is known to increase as Z_e decreases (e.g, Kobayashi et al., 2002), while this analysis assumes a constant dispersion. Preliminary verification by Hagihara et al. (2021) indicated that the standard deviation of the random error significantly increases as Z_e falls below -15 dBZ. Therefore, it is difficult to obtain reliable slope for thin cirrus clouds using the PCA because thin cirrus clouds near the tropopause typically have Z_e values below -20 dBZ (c.f. Fig. 1a).

265

https://doi.org/10.5194/egusphere-2025-4819
Preprint. Discussion started: 9 October 2025

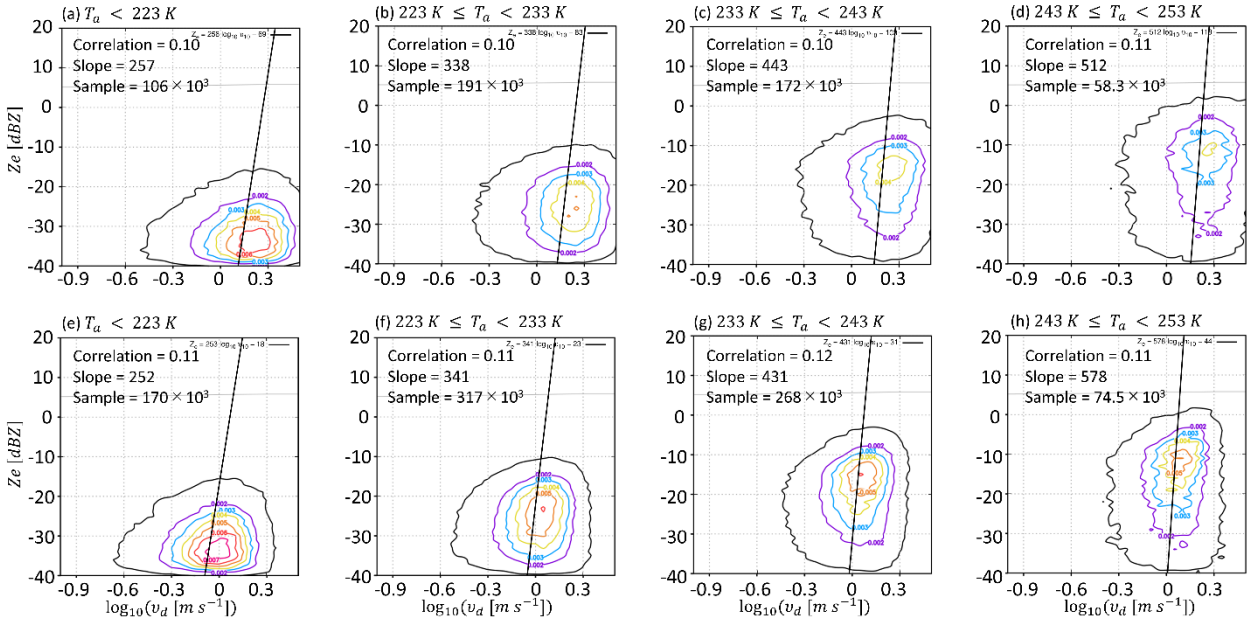

Figure 7. The same as Fig. 1 except for the post-processing. Random error, following Gaussian distribution, was added to measured Doppler velocity to emulate the 20 km observation window mode. Upper figures present the Z_e–log10v_d diagrams with the original integration mode and lower figures present Z_e–log10v_d diagrams with the pseudo-30 km integration mode.

3.4 Antenna mispointing

It is known that even a very small change in the pointing angle significantly influences the estimated vertical motion due to very high on-orbit satellite velocity and satellite height (Battaglia and Kollias, 2015; Scarsi et al., 2024). This error is referred to as the antenna mispointing error $\delta_{v,mis}$. For instance, in case of CPR with the satellite velocity of approximately 7.6 km s^{-1}, $\delta_{v,mis}$ ~ 0.5 m s^{-1} is expected to be induced by only a 0.0057 ° of antenna mispointing (Scarsi et al., 2024). Thus, the L1 products need to be revised to sufficiently correct this arising issue (Kollias et al., 2023).

In practice, degree of this error in the measured Doppler velocity can be indirectly estimated in reference to the measured Doppler velocity at surface $v_{dm,sfc}$ because vertical motion should be zero at surface (Kollias et al., 2023). After the launch, this empirical correction successfully works to reduce the systematic error in the measured Doppler velocity. The JAXA L2 products of 1 km and 10 km integration modes were made after the correction process to the L1 product with the original horizontal resolution. Minor error remains depending on seasons, latitudes, and topography (Puigdomènech Treserras et al., 2025) since the CPR observations have not been sufficiently accumulated after the launch.

The plausible range of the uncertainties in CPR mispointing error was estimated with reference to the L2 product. In the L2 product, the mispointing error is corrected by subtracting the Doppler velocity at the surface bin $v_{dm,sfc}$ from the measured Doppler velocity v_{dm}, as follows:

https://doi.org/10.5194/egusphere-2025-4819
Preprint. Discussion started: 9 October 2025

$$v_{dc} = v_{dm} - v_{offset}, \quad (16)$$

$$v_{offset} \sim v_{dm,sfc}, \quad (17)$$

$$\delta_{v,mis} = v_{offset} + \Delta\delta_{v,mis}, \quad (18)$$

where v_{dc} is the corrected Doppler velocity, $\Delta\delta_{v,mis}$ is the residual of the correction, and v_{offset} is a correction offset obtained from the surface bin (nb_{sfc}). The offset values v_{offset} in the JAXA L2 product are determined so that the 100-km along track moving average of the surface Doppler velocity $v_{dc,sfc}$ becomes zero. This exclude cases where strong cloud attenuation occurs or where surface radar cross-section is close to saturation during the moving average calculation.

Figure 8 shows the horizontal distribution of the monthly mean v_{offset} for January 2025. The v_{offset} varies periodically with the satellite's orbit around the Earth, which is thought to result from slight deviations in the antenna pointing direction from its original design, caused by solar heating of the CPR main reflector and surrounding components. This periodicity is characterized by an increase in v_{offset} when the satellite passes over the sunlit hemisphere (i.e., at the descending node), and a decrease when it passes over the night hemisphere (i.e., at the ascending node). Smooth latitudinal variations in v_{offset} over the ocean reasonably reflect antenna mispointing. In contrast, spotty and large v_{offset} values over the land (e.g., the Amazon Basin) are likely contaminated by additional noise due to inhomogeneous radar reflections from varying land surface conditions. Therefore, $\Delta\delta_{v,mis}$ is expected to vary depending on both latitude and land surface characteristics.

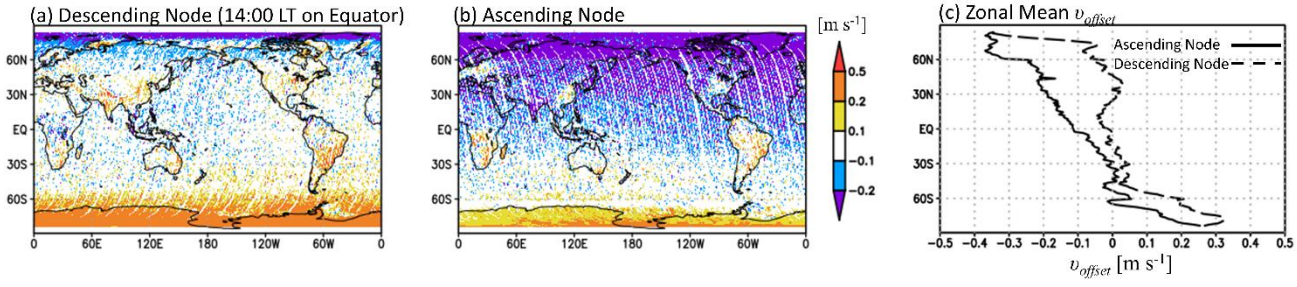

Figure 8. The offset values in (a) the descending node, (b) ascending node, and (c) their zonal mean values.

The corrected doppler velocities at the surface bin ($v_{dc,sfc}$) contain information about both the residual of the correction and the baseline random error (cf., Section 3a and 3b). The behavior of the residual in January 2025 was examined by sorting $v_{dc,1km,sfc}$ by region and orbit direction (ascending or descending). For reference, Fig. 9 presents the PDF of $v_{dc,1km,sfc}$ derived from the ascending node over the ocean between 30°S and the equator. In general, the PDF resembles a Gaussian distribution with a mean close to zero. Hence, this study employs Gaussian fitting to the PDFs under the various conditions to derive a representative range of residuals.

Note that the median of the PDF is slightly negative (Fig. 9) because $v_{dc,1km,sfc}$ values above 3 m s^{-1} are unfolded (Hagihara et al., 2021). In addition, the tails of the PDF are wider than those of a Gaussian distribution (Fig. 9), indicating the presence of

https://doi.org/10.5194/egusphere-2025-4819
Preprint. Discussion started: 9 October 2025

a significant number of outliers. Therefore, fitting a Gaussian distribution using the standard deviation of the PDF yields a profile that significantly diverges from the original distribution.

Given the unfolded doppler velocities and the presence of outliers, the region around the median is assumed to be the most reliable for Gaussian fitting. Accordingly, in this study, the standard deviation of the Gaussian distribution was estimated by fitting a parabola to four consecutive bins centered around the median, utilizing the symmetry of the Gaussian distribution, as follows:

$$PDF\left(v_{dc,1km,sfc}\right) = a_{fit}v_{dc,1km,sfc}^2 + c_{fit}, \quad (19)$$

$$\sigma_{fit} = \frac{1}{\sqrt{2\pi}PDF(0)}. \quad (20)$$

The standard deviation of the fitted Gaussian distribution (σ_{fit} = 0.82) is smaller than that of the original PDF (σ = 1.1) (Fig. 9), indicating that the fitting captures the core structure of the original PDF while minimizing the influence of outliers.

To evaluate the Gaussian random error in the Doppler velocity observations by the EarthCARE satellite, this study considers three major sources: (1) base errors originating from the intrinsic limitations of the instrument and perturbations in the satellite platform attitude, (2) observation window mode–dependent errors, and (3) errors associated with the correction of antenna mispointing. To decompose the total Gaussian error, the minimum error observed in the 16-km mode is assumed to represent the base error σ_{1km}. The difference between the minimum error in the 20-km mode and the base error is attributed to the difference in the observation window mode σ_{window}. Any remaining regional variations are attributed to uncertainties in the antenna mispointing correction σ_{mis}. Given that the three major sources are independent of each other, the variance of the total Gaussian error (σ_{fit}^2) can be expressed as the sum of the variances of the individual components:

$$\sigma_{fit}^2 = \sigma_{1km}^2 + \sigma_{window}^2 + \sigma_{mis}^2, \quad (21)$$

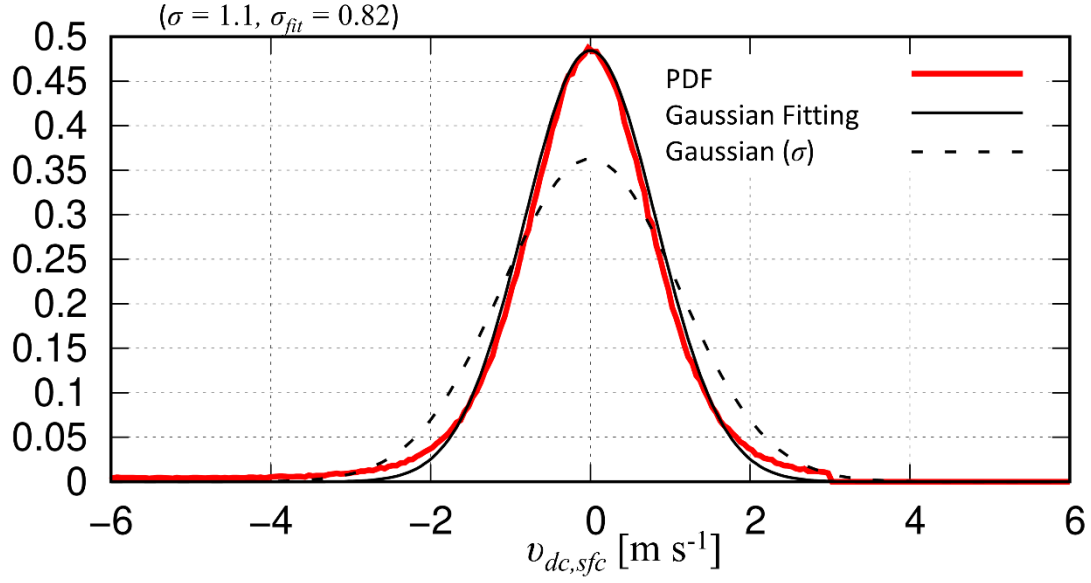

https://doi.org/10.5194/egusphere-2025-4819
Preprint. Discussion started: 9 October 2025

Figure 9. The PDF (red solid line) of $v_{dc,1km,sfc}$ in the ascending node over the ocean from 30°S to the equator. The Gaussian fit (black solid line) and a Gaussian distribution with the standard deviation derived from the PDF (black dashed line) are also shown. The standard deviations of the PDF (σ) and the fitted Gaussian (σ_{fit}) are indicated. Note that values of $v_{dc,1km,sfc}$ above 3 m s^{-1} are automatically unfolded in the JAXA L2 product, resulting in a clear drop in the PDF at $v_{dc,1km,sfc}$ = 3.

Figure 10a presents the standard deviation of the fitted Gaussian distribution for each region. In most regions, σ_{fit} does not vary significantly between the ascending and descending nodes (Figure 10b), except in a few specific areas (e.g., interior regions of China). Therefore, the ascending and descending nodes are not treated separately in the subsequent analysis. It is evident that σ_{fit} is larger between 60°S and 60°N, indicating that the 20-km observation window mode introduces greater noise compared to the 16-km mode. Among the regions, σ_{fit} mostly ranges from 0.8 to 0.9 in the 20-km mode (60°S–60°N), and from 0.4 to 0.6 in the 16-km mode (90°S–60°S and 60°N–90°N) (Fig. 10a).

The base error and the observation window mode-dependent error can be estimated from the engineering parameters of the CPR (Hagihara et al., 2023). The standard deviation of their combined contribution, $\sigma_{random}\left(=\sqrt{\sigma_{1km}^2+\sigma_{window}^2}\right)$, is given by

$$\sigma_{random} = C_{cor}\sqrt{\frac{\lambda^2}{32\pi^2 M_p \cdot \rho_{cor}^2 \cdot \left(\frac{1}{\mathrm{PRF}}\right)^2}\left\{\left(1+\frac{1}{S/N}\right)^2-\rho_{cor}^2\right\}}, \quad (22)$$

where C_{cor} is a correction factor (set to C_{cor} = 1 in this study because the target is assumed to be stationary), λ (= 3.1876 mm) is the wavelength, M_p is the number of pulse pairs within the integration length, PRF is the pulse repetition frequency, and S/N is the signal-to-noise ratio. The correlation function ρ_{cor} is defined as

$$\rho_{cor} = \exp\left\{-8\left(\frac{\pi\cdot\sigma_{vw}}{\lambda\cdot\mathrm{PRF}}\right)^2\right\}, \quad (23)$$

where σ_{vw} (= 3.85 m s^{-1}) is the Doppler velocity spectrum width, which reflects the spread caused by the satellite's motion. In practice, we assume S/N = ∞ (i.e., 1/(S/N) = 0) to derive the theoretical minimum, because surface signals may saturate and reliable estimates cannot always be obtained, even though actual N/S is greater than 0. Abnormal pixels in the L1 product were excluded using the quality flag f_{ray}, and the two neighboring footprints were averaged to match with 1 km integration data in the L2 product.

Figure 10c shows the mean σ_{random}, calculated using engineering parameters of CPR L1b data for the same period as the Level 2 product analysis. Its latitudinal distribution is similar to that of σ_{fit}, with typical values from 0.7 to 0.8 for the 20 km mode and around 0.4 for the 16 km mode. A comparison between σ_{fit} and σ_{random} further reveals anomalously small σ_{fit} values in some regions (e.g., India, eastern coastal China, and U. S. Gulf Coast). Areas where σ_{fit} falls below 0.75 in the 20 km mode, as well as those with large errors (σ_{fit} > 0.95 in the 20 km mode or σ_{fit} > 0.65 in the 16 km mode), are excluded from our analyses because the surface-reflected radar signals—and consequently the antenna mispointing error correction —are considered unreliable there.

https://doi.org/10.5194/egusphere-2025-4819
Preprint. Discussion started: 9 October 2025

Based on these estimates, the horizontal distribution of σ_{mis} is derived using Eq. (21) (Figure 10d). In the 20 km mode, σ_{mis} is mostly less than 0.6, indicating that the uncertainty associated with the antenna mispointing error correction is smaller than σ_{random} but still non-negligible. This influence can be reduced by selecting appropriate geographical regions. In particular, the 16 km mode (90°S–60°S) is highly advantageous for the present analysis, as it not only has smaller intrinsic Doppler velocity errors but also exhibits lower uncertainty in the antenna mispointing error correction.

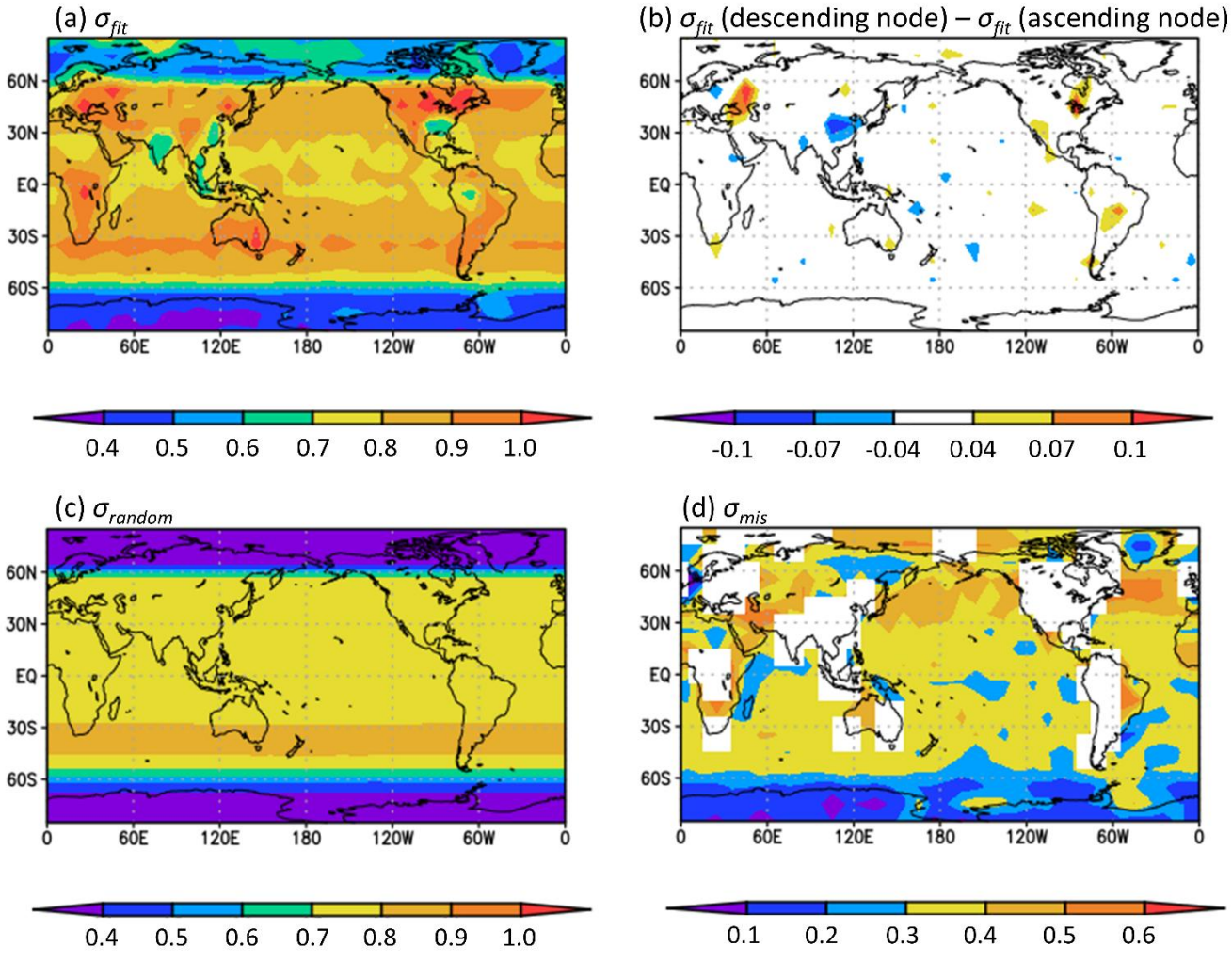

Figure 10. Horizontal distributions of (a) the standard deviation of the fitted Gaussian distribution (σ_{fit}), (b) the difference in σ_{fit} between the descending and ascending nodes, (c) the random error estimate (σ_{random}) derived from CPR engineering parameters (combining base error and observation window–mode error), and (d) the standard deviation of the residuals after the correction for antenna mispointing errors. The standard deviations are calculated within each 10°×10° grid to ensure a sufficient number of samples for Gaussian fitting.

https://doi.org/10.5194/egusphere-2025-4819
Preprint. Discussion started: 9 October 2025

North of 60° N, however, the random error associated with antenna mispointing correction remains notably large, despite the application of the 16 km mode (Fig. 10d). This elevated error can be attributed to two primary factors: anomalous surface scattering properties and deficiencies in the digital elevation model (DEM). The current correction method assumes that the surface Doppler velocity is zero, but this assumption breaks down over surfaces with exceptionally strong backscatter or sloping terrain. For example, over sea ice in the Arctic Ocean or along the Antarctic coast, surface echoes occasionally become strong; in such cases, the observed surface Doppler velocity tend to approach zero regardless of the actual pointing error. This leads to large variability in v_{offset}, which in turn increases σ_{mis}. Similarly, unusually small σ_{fit} values observed over land may also reflect the breakdown of this assumption under anomalous scattering conditions. It should be noted that, in the correction procedure, cases with such strong surface echoes are excluded before applying the moving average to the surface Doppler velocity, so this effect is likely mitigated.

Another contributing factor is the lack of reliable topographic data in some polar regions, such as northern Greenland, within the DEM. This is a critical limitation for antenna mispointing correction methods that utilize surface Doppler velocities, and such inaccuracies also impair ground clutter detection. A preliminary announcement regarding this issue is available on the JAXA website. Although these known problems are expected to be resolved in the next major product release, scheduled for December 2025, they currently degrade the overall quality of the data analysis in this study. To mitigate their impact, regions with large or unreliable σ_{fit} values have been excluded, as indicated by the mask shown in Figure 10d.

4 Revised Analysis Method

By taking into account the random error in the L2 product mentioned above, it was found that the PCA analysis proposed based on ground-based Doppler radar observations suffers from significant error propagation caused by the logarithmic transformation and positive-value sampling. To address this issue, this study introduces a more robust method to extract the representative slope on the Z_e–$\log_{10}v_d$ diagram as an alternative to PCA. Specifically, for each Z_e bin, we compute the median of v_d and then take its logarithm. Since the Doppler velocity contains significant random noise, especially after the $\log_{10}$ transformation, this procedure minimizes the bias caused by skewed noise propagation. The resultant set of points represents the central tendency of the Z_e–$\log_{10}v_d$ relationship, from which a robust slope can be derived. When estimating the slope, the median values at each Z_e are weighted according to the observation frequency of each Z_e, rather than being treated equally. In the case of EarthCARE observations, an additional weight proportional to the inverse of the variance (i.e., a reliability weight) is also applied, since the random noise in v_d increases as Z_e decreases (e.g., Hagihara et al., 2021).

In the initial approach, cloud layers were selected based on the condition that both the vertical gradients of Z_e and $\log_{10}v_d$ were positive between two adjacent levels (Eqs. 8-10). However, such local gradients of $\log_{10}v_d$ are susceptible to random noise and may not consistently represent physically meaningful structures. The apparent inconsistencies in the results

https://doi.org/10.5194/egusphere-2025-4819
Preprint. Discussion started: 9 October 2025

obtained by the original analysis method (Fig. 3) are partly attributed to this sampling error. To address this, the sampling criterion was revised to utilize only the vertical gradient of Z_e.

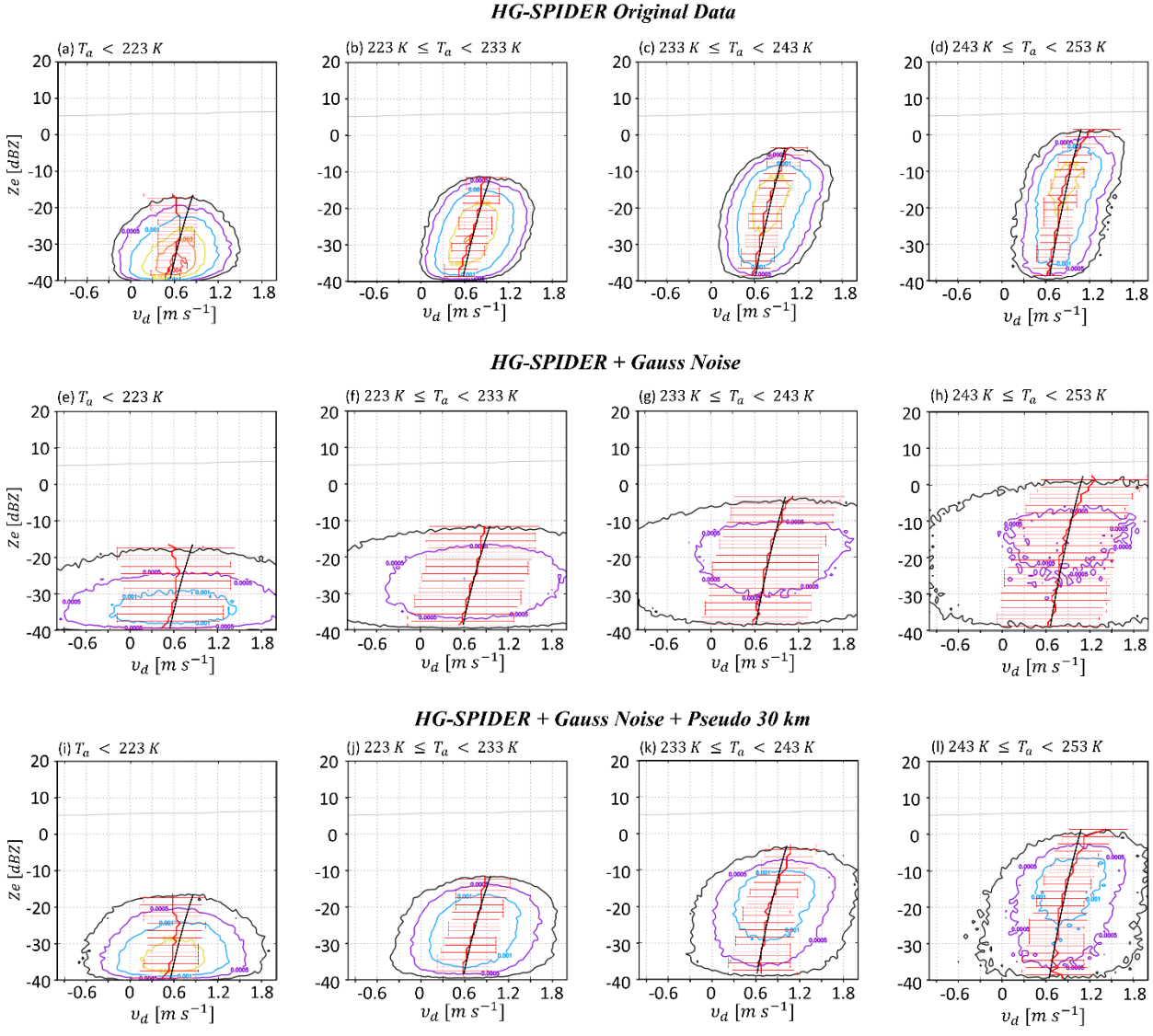

Figure 11. Bin-integrated joint probability density functions (color contours) of Z_e and v_d derived from (top row) the original HG-SPDIER observations, (middle row) HG-SPDIER observations with the prescribed Gaussian noise (σ = 1 m s^{-1}), and (bottom row) HG-SPIDER observations with the Gaussian noise under the pseudo-30 km integration mode. The black contour encloses approximately 90% of the samples. The red line indicates the median v_d in each Z_e bin, and the error bars represent the 25th and 75th percentiles. The black lines denote the slope derived from PCA applied to the original HG-SPIDER observations.

https://doi.org/10.5194/egusphere-2025-4819
Preprint. Discussion started: 9 October 2025

Figure 11 shows a comparison between the PCA-derived slope and the curve formed by connecting the median v_d values for each Z_e bin. It is confirmed that the median-based curve closely follows the PCA-derived slope, even when the JPDF becomes highly dispersed due to the added Gaussian noise. This behavior remains consistent regardless of the choice of the integration mode. Even after the logarithmic transformation, the new method provides slope values consistent with those derived the PCA across each atmospheric temperature (Fig. 12). However, when the random error is large, it becomes difficult to accurately reproduce the slope values (Fig. 12). In particular, the tendency of the slope to increase with rising atmospheric temperature is no longer captured. This inconsistency is not resolved even when using the pseudo-30 km mode (not shown). This suggests that in regions with higher levels of random error (Section 3c), a larger sample size may be required to obtain reliable slope estimates.

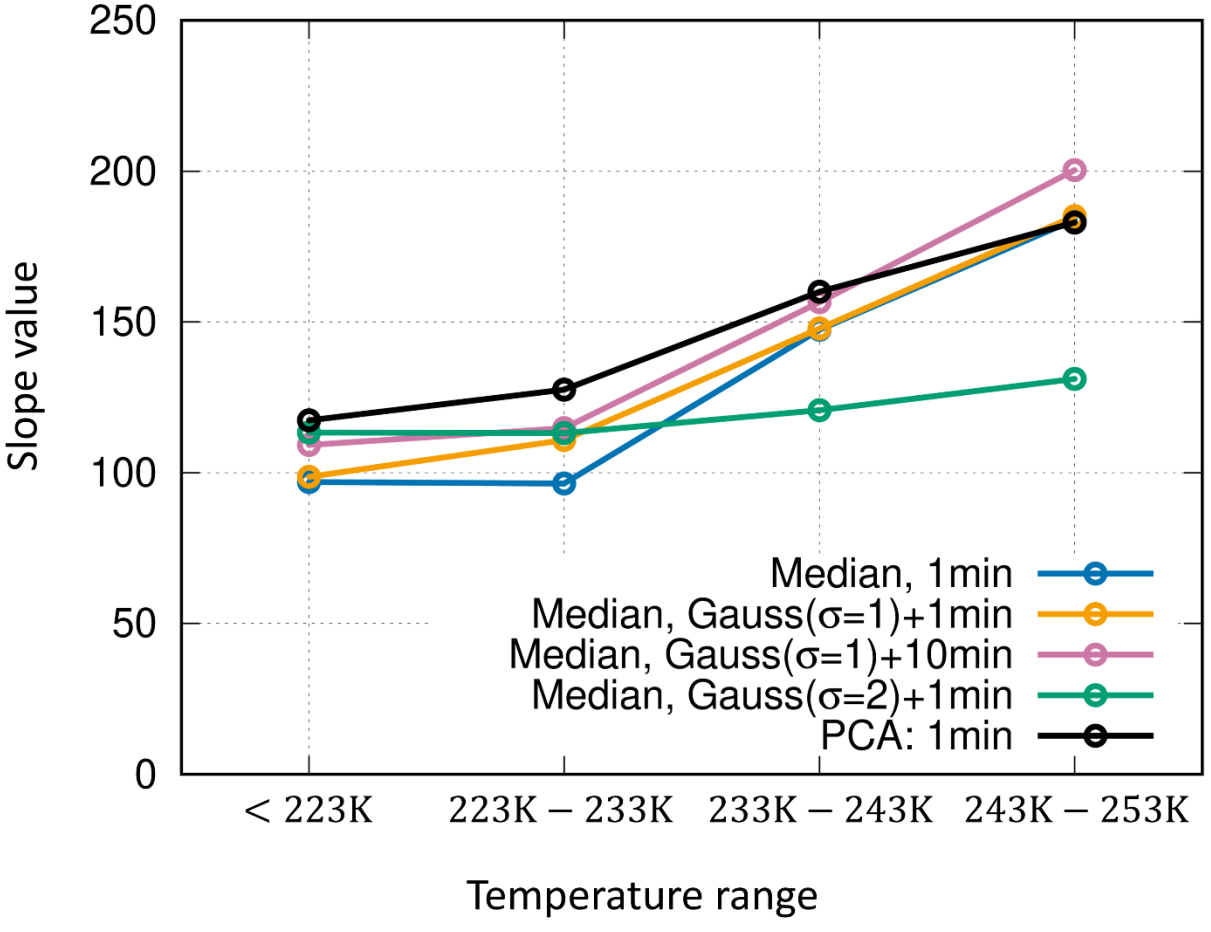

Figure 12. Transition of slope values across the four different atmospheric temperature ranges. The black line shows valued derived from PCA. Colored lines represent those obtained using the new method applied to HG-SPIDER data: red (original),

https://doi.org/10.5194/egusphere-2025-4819
Preprint. Discussion started: 9 October 2025

green (with the prescribed Gaussian noise), blue (with the prescribed Gaussian noise under the pseudo-30 km mode), and magenta (with stronger Gaussian noise, $\sigma = 2$).

5 Analysis using EarthCARE Satellite Observations

5.1 Data Processing

In the global analysis, this study focuses on cloud layers below 16 km altitude (approximately 100 hPa over the tropics), since the definition of cirrus clouds in the growth mode becomes invalid due to the temperature inversion near the tropopause. As the cirrus cloud fraction above 16 km is sufficiently small—less than 0.01 (Fig. 7 in Seiki and Nagao, 2024)—this sampling choice does not affect the conclusions. Atmospheric temperature and horizontal wind field from the NCEP-FNL product were used, consistent with the analysis employing HG-SPIDER observations.

In global analyses, it is essential to account for the dependence of terminal fall velocities on atmospheric thermodynamic conditions to accurately retrieve microphysical properties, because terminal velocities are sensitive to air density, which affects aerodynamic drag. This dependence introduces spatial variability in Doppler velocity that is unrelated to microphysical processes themselves. To mitigate this, a simplified correction scheme for ice particle terminal velocities, originally proposed by Beard (1980), was employed:

$$v_{t,ref} = v_t \, f_{v_t}, \tag{24}$$

$$f_{v_t} = \left(\frac{\rho_a}{\rho_{a,ref}}\right)^{1/2}, \tag{25}$$

where the reference atmospheric conditions are defined as $\rho_{a,ref} = 0.98$ kg m^{-3}, $T_{a,ref} = 273$ K, and $p_{ref} = 770$ mb. Accordingly, the Doppler velocity was corrected to the reference atmosphere by multiplying $\sqrt{\rho_a} \sim \sqrt{\frac{p}{R_{air} T_a}}$, for simplicity, where p is atmospheric pressure and R_{air} is the specific gas constant for dry air.

Note that Eq. (24) is valid for ice particles with Reynolds numbers greater than 1000.0. However, small ice crystals in cirrus clouds typically have Reynolds numbers in the range of 1 to 100, where the assumption may not strictly hold.

Figure 13 presents the annual and zonal mean values of the correction factor computed using the NCEP-FNL dataset. Even at the same temperature level, the correction factor varies with latitude, indicating that the influence of thermodynamic conditions on global Doppler velocity analyses is non-negligible. Accordingly, applying the correction factor helps reduce this influence, allowing clearer interpretation of Doppler velocity variations due to shifts in dominant microphysical processes.

https://doi.org/10.5194/egusphere-2025-4819
Preprint. Discussion started: 9 October 2025

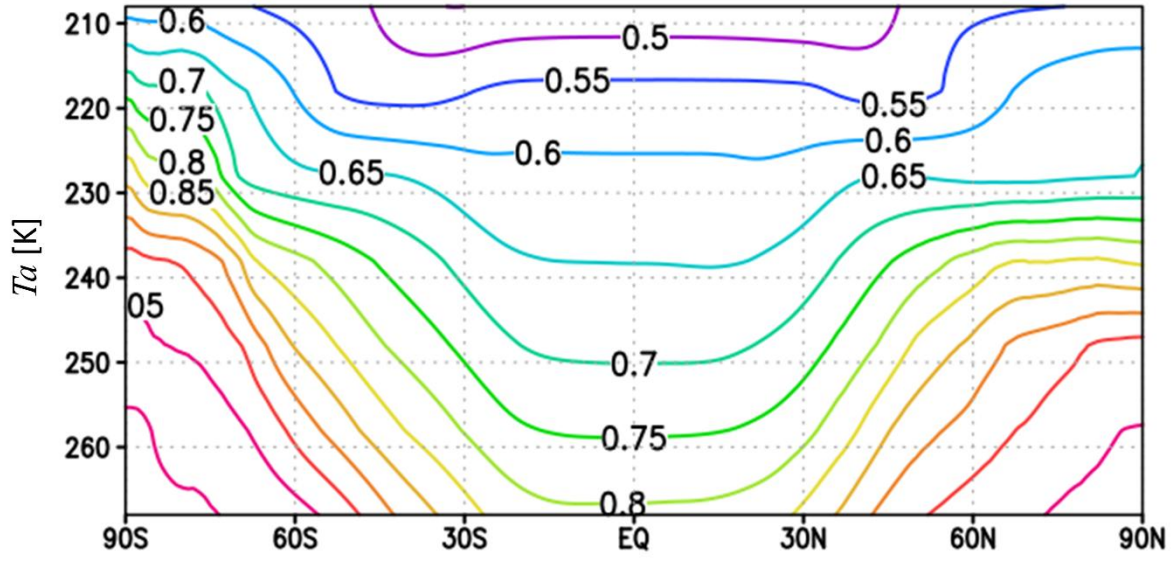

Figure 13. Annual and zonal mean values of the correction factor ($\sqrt{\rho_a} \sim \sqrt{\frac{p}{R_{air} T_a}}$), computed using the NCEP-FNL dataset. Atmospheric temperature is used as the vertical coordinate.

Figure 14 compares the PDFs of Doppler velocities across different temperature ranges. When the terminal velocity correction is applied, the standard deviation decreases, which is a natural consequence of the overall reduction in terminal velocity (as shown in Fig. 13). However, the coefficient of variation (CV) increases globally after applying the terminal velocity correction, which may indicate enhanced regional contrasts in microphysical characteristics. Nevertheless, in low-temperature regions near the tropopause where radar reflectivity is weak, the increased influence of noise (shown later) and the reduction in mean Doppler velocity due to the correction may artificially elevate CV. Therefore, the apparent increase in CV should be interpreted with caution, as it may reflect both physical and non-physical contributions.

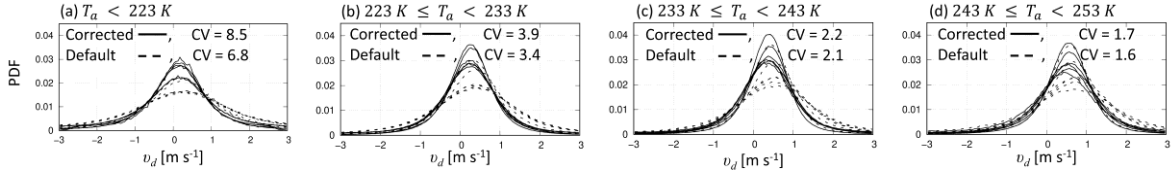

Figure 14. Probability density functions (PDFs) of Doppler velocities with (solid lines) and without (dashed lines) the correction, shown across different temperature ranges. Each PDFs was calculated over 30°-wide latitudinal bands spanning from 90°S to 90°N. The coefficient of variation (CV) is also indicated.

https://doi.org/10.5194/egusphere-2025-4819
Preprint. Discussion started: 9 October 2025

5.2 Global analysis

Joint probability density functions of Z_e and v_d were analyzed in 30°-wide latitudinal bands to ensure a sufficient sample number of cirrus clouds. Figure 15 presents the comparison of the joint PDFs in the Northern Hemisphere. It was found that the joint PDFs from EarthCARE satellite observations are quite noisy, as was similarly seen in the HG-SPIDER observations with the prescribed Gaussian noise (e.g., Figs. 11i-l). Additionally, the random noise increases as Z_e (signal-to-noise ratio) decreases. Nevertheless, the median-based curves successfully capture a moderate increase in Doppler velocity with increasing Z_e, despite the large noise. Notably, the median-based curves are mostly parallel to those obtained from the HG-SPIDER observations. These characteristics are consistently observed across all temperature ranges, indicating that the revised analysis method proposed in Section 4 is effective.

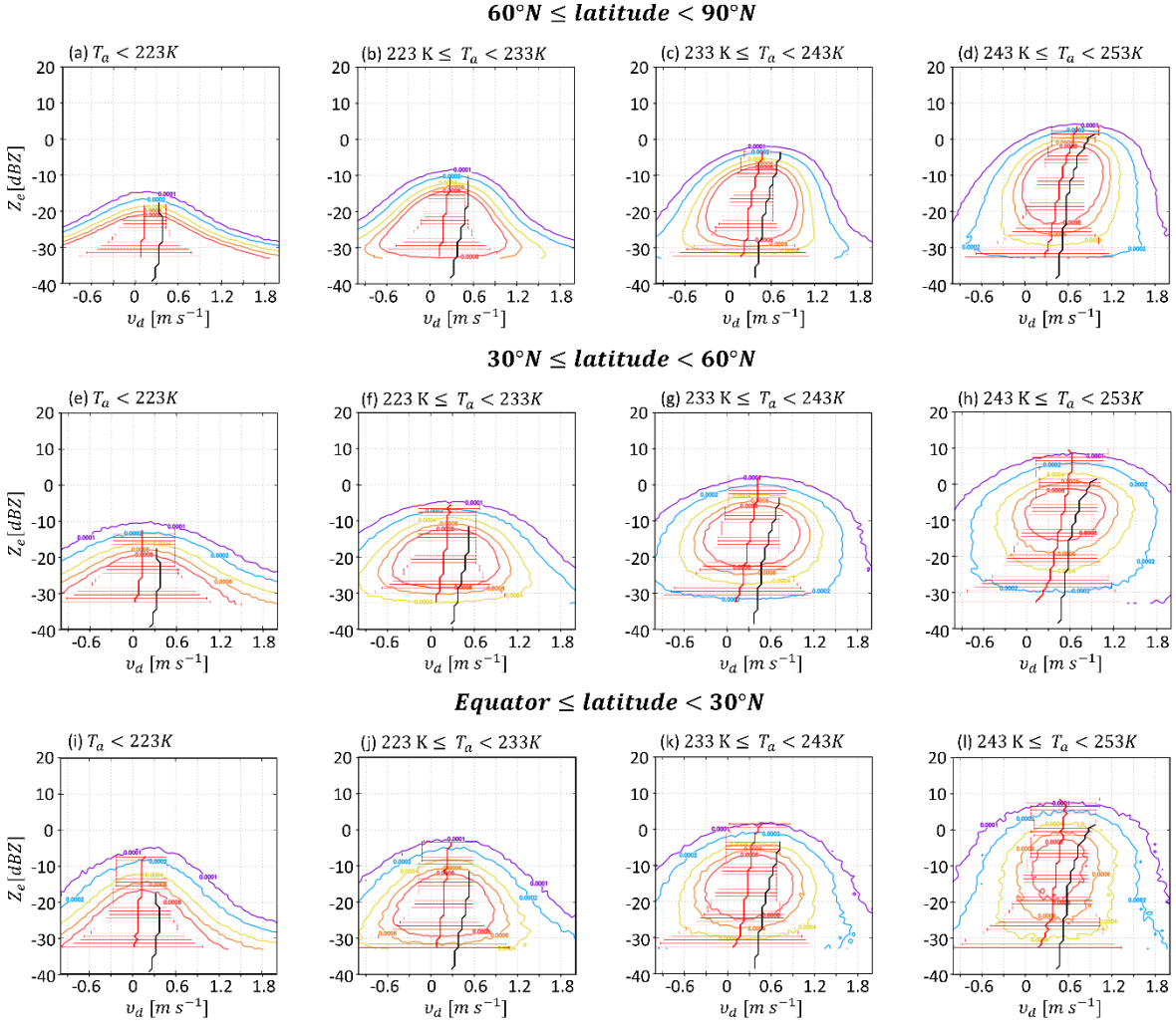

https://doi.org/10.5194/egusphere-2025-4819
Preprint. Discussion started: 9 October 2025

Figure 15. Same as Fig. 11 but for the EarthCARE satellite observations. The joint PDFs of Z_e and v_d are analyzed over 30°-wide latitudinal bands from the Equator to the North Pole. The black lines denote the median-based curves from the HG-SPIDER observations, which have been postprocessed using the density correction (Eqs. 24-25).

In terms of quantitative evaluation, systematic differences in the median-based curves between the EarthCARE and HG-SPIDER observations are evident. The discrepancy is approximately 0.3 m s^{-1} near the tropopause and gradually deceases with decreasing altitude. This difference likely arises from the disparity in antenna pointing direction between the EarthCARE CPR and HG-SPIDER, which may be attributed to (i) the difference between the gravitational vector and the normal vector of the Earth's surface, or (ii) a misalignment of the ground-based Doppler radar.

In Tokyo, the gravity vector is slightly tilted relative to the surface normal of the Earth's ellipsoid. According to historical geodetic data from 1956 observed in Azabu, Tokyo, the deflection of the vertical in the east-west direction was approximately −7.87 arcseconds (-0.0022 degrees) (Torao, 1956), meaning that the gravity vector is tilted slightly westward compared to the ellipsoidal normal. Here, the ellipsoidal normal corresponds to the viewing direction of the EarthCARE CPR, while the gravity vector corresponds to the pointing direction of the HG-SPIDER radar.

Figure 16 shows the annual mean vertical profile of the easterly wind component (U) and the associated Doppler velocity error (δ_{tilt}) caused by a tilted angle of the pointing direction of the HG-SPIDER compared to the ellipsoidal normal ($\theta_{tilt,}$ defined as positive eastword). The error was estimated using the following relationship:

$$\delta_{tilt} = -U \sin\theta_{tilt} \approx -U\theta_{tilt}. \quad (26)$$

The errors originating from the tilted gravity vector are found to be less than 1 cm s^{-1}. Therefore, the westward tilt of the gravity vector cannot account for the discrepancy observed in the median Doppler velocity curves (Fig. 15). We conclude that the discrepancy most likely originates from a misalignment of the ground-based Doppler radar, estimated to be approximately -0.7 degree. After applying this tilt correction, the median-based curve from the HG-SPIDER observations shows excellent agreement with the EarthCARE satellite observations between 30° N and 60° N (Fig. 17): the differences in median v_d values at each Z_e bin are mostly within 5 cm s^{-1} across all four temperature ranges.

Note: The HG-SPIDER system has not undergone regular calibration for pointing angle since its installation. Such a degree of misalignment is plausible due to long-term mechanical shifts in the radar container and frequent seismic activity in Japan.

https://doi.org/10.5194/egusphere-2025-4819
Preprint. Discussion started: 9 October 2025

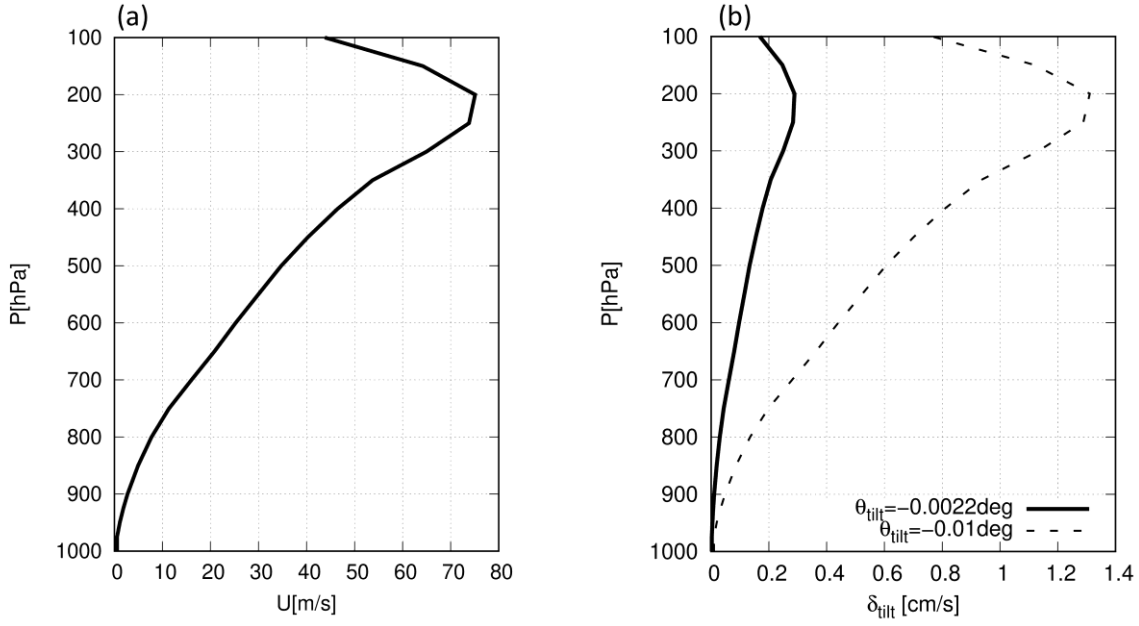

Figure 16. (a) The annual mean vertical profile of easterly wind (*U*) and (b) errors in Doppler velocity (δ_{tilt} [cm s^{-1}]) due to tilted pointing angle (θ_{tilt}, Easterly positive).

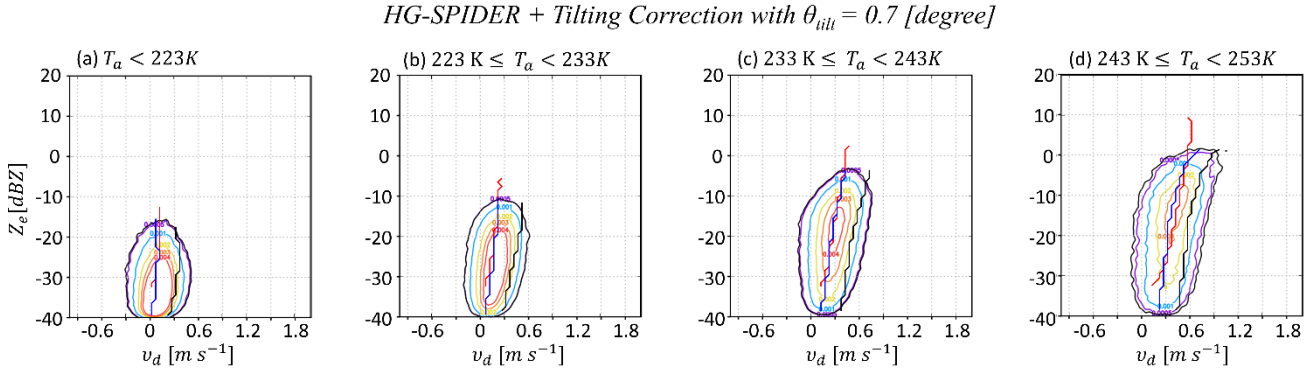

Figure 17. Same as Fig. 11, except for the HG-SPIDER observations with the antenna tilt correction applied (θ_{tilt} = -0.7°). The blue lines represent the slopes derived from the median-based curves. The black and red lines denote the median-based curves from the original HG-SPIDER observations and the EarthCARE satellite observations between 30°N and 60°N, respectively. Doppler velocities have been postprocessed using the density correction (Eqs. 24-25).

Finally, the regional variation in the representative slope value is summarized in Figure 18. HG-SPIDER observations, roughly adjusted to align with the EarthCARE satellite data, are also shown. The slope values from the EarthCARE

https://doi.org/10.5194/egusphere-2025-4819
Preprint. Discussion started: 9 October 2025

observations between 30°N and 60°N are nearly identical to those derived from HG-SPIDER, demonstrating the robustness of the revised analysis method, even when using Doppler velocity data with high noise levels.

In cirrus clouds, the slope values consistently increase with rising atmospheric temperature, indicating that temperature sensitivity exceeds regional variability. Specifically, smaller slope values are observed at temperatures between 243 K and 253 K within the latitudinal bands from 30°S to the Equator, whereas larger values dominate at most atmospheric temperature ranges south of 60°S. Based on the theoretical background of the Z_e–$\log_{10}v_d$ relationship (Eqs. 11-13), this regional difference suggests that aggregation processes are more dominant in the tropical Southern Hemisphere, while vapor deposition processes prevail in the Antarctic region.

To enable more detailed regional analyses, a longer observation period is needed to increase the sample size —for instance, an annual dataset could allow a fourfold longitudinal segmentation. Furthermore, ground-based Doppler radars deployed across diverse regions (e.g., networks such as Cloudnet; Illingworth et al., 2007; Radenz et al., 2021) can be cross-calibrated using EarthCARE observations, similar to how ground-based weather radar networks were calibrated using the Tropical Rainfall Measuring Mission (TRMM) and Global Precipitation Measurement (GPM) satellite observations (e.g., Anagnostou et al., 2001; Warren et al., 2018; Louf et al., 2019; Louf and Protat, 2023). This cross-calibration will enable high-resolution radar measurements with EarthCARE-equivalent accuracy.

https://doi.org/10.5194/egusphere-2025-4819
Preprint. Discussion started: 9 October 2025

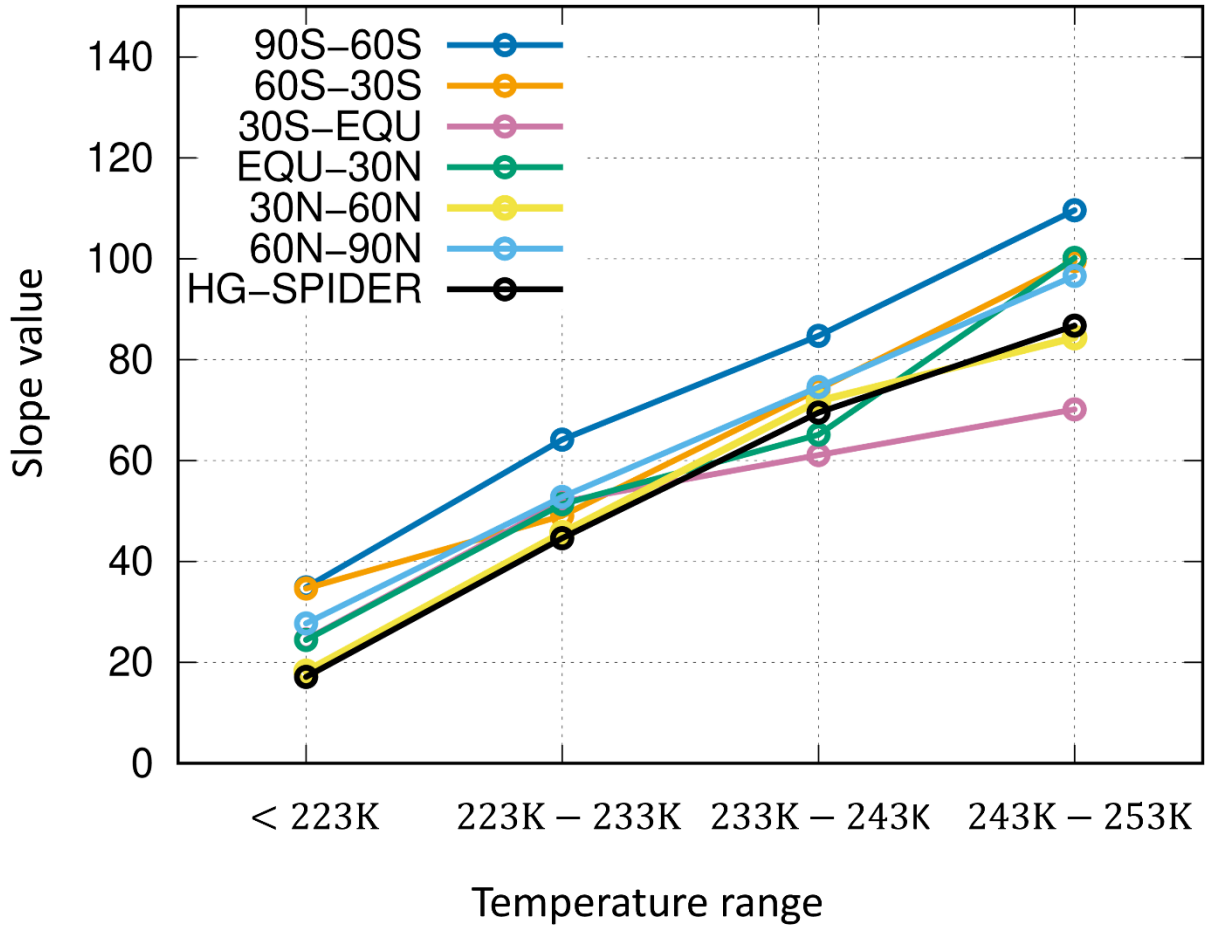

Figure 18. Same as Fig. 12, except for the EarthCARE observations. Colored lines indicate representative slope values calculated from the median-based curve. The black line shows values derived from the HG-SPIDER observations with the antenna tilt correction applied (θ_{tilt} = -0.7°).

6 Discussion

The method presented in this study assumes that the radar reflectivity factor (Z_e) follows Rayleigh scattering (Eq. 1) in thin cirrus clouds, and Mie scattering (Eq. 7) in the deeper portions of cirrostratus clouds, depending on particle size range. However, it is challenging to determine whether the observed change in the representative slope originates from the transition between Rayleigh and Mie scattering regimes, or from a shift in the dominant cloud microphysical processes. Additionally, attenuation of radar signals in the deeper region of cirrostratus clouds is non-negligible when considering the cause of changes in Z_e.

https://doi.org/10.5194/egusphere-2025-4819
Preprint. Discussion started: 9 October 2025

These issues are mitigated when using radars with longer wavelengths, such as the Ku- or Ka-band radars onboard the GPM satellite. In this wavelength range, Rayleigh scattering alone is generally sufficient to describe particle interactions, and signal attenuation becomes negligible even in deeper cloud layers. Applying this method to EarthCARE–GPM coincident observations (Aoki et al. 2025), as well as to the planned Ku-band Doppler precipitation radar under the Precipitation Measuring Mission (Nakamura and Furukawa, 2023), offers the potential to capture particle growth deeper inside clouds in future studies.

7 Summary

This study applies a method for identifying ice-particle growth in cirrus clouds to global satellite observations. The analysis uses the ratio of the change in equivalent radar reflectivity factor (Z_e) to the change in Doppler velocity (v_d) on a common logarithmic scale — $\left(\frac{\Delta Z_e}{\Delta \log_{10} v_d}\right)$, hereafter referred to as the slope —as a quantitative indicator of dominant cloud microphysical processes in cirrus clouds. The objective is to derive the climatological characteristics of cirrus cloud growth by statistically determining representative slope values across different temperature ranges.

A prior study defined the representative slope as the first principal component in the joint probability density function (joint PDF) of Z_e and $\log_{10} v_d$ (i.e., the Z_e–$\log_{10} v_d$ diagram), using Principal Component Analysis (PCA). However, this method was found to be significantly affected by non-negligible random noise in Doppler velocity measurements from the EarthCARE satellite. To evaluate the error factors, accurate in-situ ground-based Doppler radar observations at a single site and globally distributed noise-prone satellite observations serve as complementary datasets.

This study investigated three major error sources: integration length, two types of observation window modes, and antenna mispointing correction. The impact of integration length on PCA was found to be relatively small. In contrast, larger observation windows and antenna mispointing correction introduces substantial random noise in v_d. Additionally, the base-level noise itself has a non-negligible standard deviation (e.g., up to 1.3 m s^{-1} of random noises is tolerated under mission requirements, Wehr et al. 2023). Further degradation occurs due to error propagation in the $\log_{10}$ transformation.

Given the inevitability of these errors, a revised analysis method is proposed: the random noise in v_d is mitigated by taking the median value of v_d within each Z_e bin of the joint PDF, followed by applying the $\log_{10}$ transformation to the median. This approach effectively suppresses the influence of random errors on the derived representative slope values.

Sensitivity analysis using ground-based radar data showed that the required sample size for obtaining reliable representative slope values depends on the noise level. With three months of EarthCARE data, a latitudinal sampling width of 30° was found sufficient for stable representative slope estimates.

Using the revised method, representative slope values obtained under the particularly noisy 20-km observation window mode were found to closely match those derived from HG-SPIDER observations. This result also suggests that long-term ground-based observations at a single site can reproduce Z_e–$\log_{10} v_d$ diagrams of comparable quality to satellite data. As an

https://doi.org/10.5194/egusphere-2025-4819
Preprint. Discussion started: 9 October 2025

additional outcome, the analysis indicates that antenna mispointing errors, which are usually difficult to calibrate in ground-based Doppler radars, can potentially be corrected by reference to satellite observations.

A relationship between the representative slope and atmospheric temperature had already been identified at the ground site in Koganei, Tokyo. EarthCARE's global observations now demonstrate, for the first time, that this relationship is universal: the representative slope increases systematically with temperature across all latitude bands. Regional differences in representative slope values are minor, but still provide distinctive signatures of local microphysical processes.

Future work with extended observation periods will allow investigations of finer regional and seasonal variability, as well as the role of environmental factors such as aerosols in modulating cirrus particle growth.

Appendix A Ground Clutter Removal and Z_e Threshold

In the JAXA L2 product (L2A/CPR_ECO/vBa), ground clutter is flagged using the variable f_{ze}. Nevertheless, contamination by ground clutter remains in the product, even after postprocessing with the f_{ze} quality flag.

Figure A1 shows the joint PDF of Z_e and v_d for cirrus clouds observed south of 60°S during January 2025 by EarthCARE. A spurious mode appears at Z_e values greater than 5 dBZ and $|v_d| < 0.6$ m s^{-1}. Cloud layers with such strong radar reflectivity should exhibit higher ice terminal velocities. Therefore, this spurious mode —centered around zero Doppler velocity—is interpreted as ground clutter contamination.

These signals are particularly prevalent at altitudes below 500 m above the surface. To minimize ground clutter contamination, this study excluded low-altitudes range bins from the analysis. Specifically, applying a threshold at 500 m removes 95% of this ground clutter, 1000 m removes 98%, and 1500 m removes 99%. For safety, this study only analyzed data from range bins above 1000 m.

In addition, Doppler velocities corresponding to Z_e values below -33 dBZ are found to be very noisy due to low signal-to-noise ratios, even though the minimum detectable Z_e is -35 dBZ (Wehr et al., 2023). Therefore, this study further restricted the analyzed to range bins with $Z_e \geqq$ -33 dBZ.

https://doi.org/10.5194/egusphere-2025-4819
Preprint. Discussion started: 9 October 2025

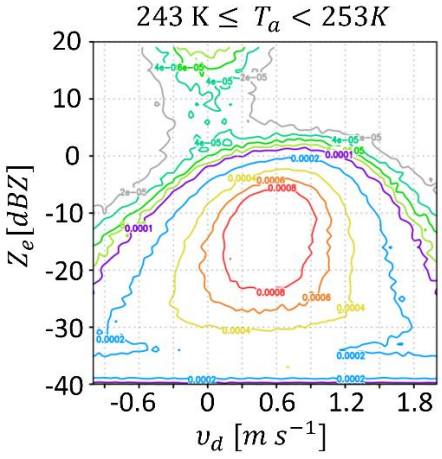

Figure A1. The joint PDF of Z_e and v_d for cirrus layers at temperatures between 243 K and 253 K, observed south of 60°S during January 2025.

Data availability

The EarthCARE CPR Level 2A product (CPR_ECO, Version vBa) and Level 1B product (CPR_NOM, Version vCa) used in this study are provided by the Japan Aerospace Exploration Agency (JAXA). The CPR_ECO L2A product was publicly released on 17 March 2025. All EarthCARE data were downloaded from the JAXA G-Portal after user registration. The HG-SPIDER observation data are currently not publicly available due to ongoing data policy development. Once the policy is finalized, the author (HH) will consider making the data available upon reasonable request. The NCEP-FNL product was obtained from https://doi.org/10.5065/D6M043C6.

Author contribution

TS downloaded and analyzed the satellite data, analyzed the ground-based observational data, and prepared the initial draft of the manuscript. HH and YH conducted ground-based Doppler radar observations, provided the corresponding data, and supported the analysis of the ground-based observations. HH, YH, and SA contributed to the analysis of satellite observations. HH, YH, SA, and AN reviewed the manuscript and provided feedback.

Competing interests

The contact author has declared that none of the authors has any competing interests.

https://doi.org/10.5194/egusphere-2025-4819
Preprint. Discussion started: 9 October 2025

Acknowledgments.

The authors thank the members in the EarthCARE Joint Mission Advisory Group and Quality Working Group for their continuous efforts in the calibration and validation of EarthCARE Level 1 products, and for summarizing known issues in both Level 1 and Level 2 products. The authors used ChatGPT (developed by OpenAI) to assist with the English language editing and translation of parts of the manuscript. The final content was carefully reviewed and edited by the authors.

Financial Support

The operation expense of the HG-SPIDER was supported by the Promotion of observation and analysis of radio wave propagation fund of the Ministry of Internal Affairs and Communications, Japan. This study was supported by the Third and Fourth Research Announcement on the Earth Observations of JAXA.

References

Anagnostou, E. N., Morales, C. A., and Dinku, T.: The Use of TRMM Precipitation Radar Observations in Determining Ground Radar Calibration Biases, Journal of Atmospheric and Oceanic Technology, https://doi.org/10.1175/1520-0426(2001)018%3C0616:TUOTPR%3E2.0.CO;2, 2001.

Aoki, S., Kubota, T., and Turk, F. J.: Exploring vertical motions in convective and stratiform precipitation using spaceborne radar observations: Insights from EarthCARE and GPM coincidence dataset, under review at Atmospheric Measurement Techniques, https://doi.org/10.5194/egusphere-2025-3596, 2025.

Battaglia, A. and Kollias, P.: Using Ice Clouds for Mitigating the EarthCARE Doppler Radar Mispointing, IEEE Transactions on Geoscience and Remote Sensing, 53, 2079–2085, https://doi.org/10.1109/TGRS.2014.2353219, 2015.

Beard, K. V.: The Effects of Altitude and Electrical Force on the Terminal Velocity of Hydrometeors, Journal of the Atmospheric Sciences, 37, 1363–1374, 1980.

Hagihara, Y., Ohno, Y., Horie, H., Roh, W., Satoh, M., Kubota, T., and Oki, R.: Assessments of Doppler Velocity Errors of EarthCARE Cloud Profiling Radar Using Global Cloud System Resolving Simulations: Effects of Doppler Broadening and Folding, IEEE Transactions on Geoscience and Remote Sensing, 1–9, https://doi.org/10.1109/TGRS.2021.3060828, 2021.

https://doi.org/10.5194/egusphere-2025-4819
Preprint. Discussion started: 9 October 2025

Hagihara, Y., Ohno, Y., Horie, H., Roh, W., Satoh, M., and Kubota, T.: Global evaluation of Doppler velocity errors of EarthCARE cloud-profiling radar using a global storm-resolving simulation, Atmospheric Measurement Techniques, 16, 3211–3219, https://doi.org/10.5194/amt-16-3211-2023, 2023.

Hashino, T., Satoh, M., Hagihara, Y., Kubota, T., Matsui, T., Nasuno, T., and Okamoto, H.: Evaluating cloud microphysics from NICAM against CloudSat and CALIPSO, Journal of Geophysical Research: Atmospheres, 118, 7273–7292, https://doi.org/10.1002/jgrd.50564, 2013.

Hashino, T., Satoh, M., Hagihara, Y., Kato, S., Kubota, T., Matsui, T., Nasuno, T., Okamoto, H., and Sekiguchi, M.: Evaluating Arctic cloud radiative effects simulated by NICAM with A-train, Journal of Geophysical Research: Atmospheres, 121, 7041–7063, https://doi.org/10.1002/2016JD024775, 2016.

Hashino, T., Satoh, M., Kubota, T., Koshiro, T., Okamoto, K., Hagihara, Y., Okamoto, H., and Seiki, T.: A Sub-Grid Precipitation Generator Based on NICAM for Simulating Cloud Radar Signals With GCMs, Journal of Geophysical Research: Atmospheres, 130, e2024JD042597, https://doi.org/10.1029/2024JD042597, 2025.

Horie, H., Iguchi, T., Hanado, H., Kuroiwa, H., Okamoto, H., and Kumagai, H.: Development of a 95-GHz Airborne Cloud Profiling Radar (SPIDER) --Technical Aspects--, IEICE TRANSACTIONS on Communications, E83-B, 2010–2020, 2000.

Illingworth, A. J., Hogan, R. J., O'Connor, E. J., Bouniol, D., Brooks, M. E., Delanoé, J., Donovan, D. P., Eastment, J. D., Gaussiat, N., Goddard, J. W. F., Haeffelin, M., Baltink, H. K., Krasnov, O. A., Pelon, J., Piriou, J.-M., Protat, A., Russchenberg, H. W. J., Seifert, A., Tompkins, A. M., Zadelhoff, G.-J. van, Vinit, F., Willén, U., Wilson, D. R., and Wrench, C. L.: Cloudnet, https://doi.org/10.1175/BAMS-88-6-883, 2007.

Illingworth, A. J., Barker, H. W., Beljaars, A., Ceccaldi, M., Chepfer, H., Clerbaux, N., Cole, J., Delanoë, J., Domenech, C., Donovan, D. P., Fukuda, S., Hirakata, M., Hogan, R. J., Huenerbein, A., Kollias, P., Kubota, T., Nakajima, T., Nakajima, T. Y., Nishizawa, T., Ohno, Y., Okamoto, H., Oki, R., Sato, K., Satoh, M., Shephard, M. W., Velázquez-Blázquez, A., Wandinger, U., Wehr, T., and Zadelhoff, G.-J. van: The EarthCARE Satellite: The Next Step Forward in Global Measurements of Clouds, Aerosols, Precipitation, and Radiation, Bulletin of the American Meteorological Society, 96, 1311–1332, https://doi.org/10.1175/BAMS-D-12-00227.1, 2015.

Japan Aerospace Exploration Agency: EarthCARE/CPR L2A CPR one-sensor Echo Product, Version vBa, 2024, [data set], https://doi.org/10.57746/EO.01jdvd0xm10ema4rxwbpcd0dn1.

https://doi.org/10.5194/egusphere-2025-4819
Preprint. Discussion started: 9 October 2025

Japan Aerospace Exploration Agency: EarthCARE/CPR L1B CPR one-sensor Received Echo Power Product, Version vCa, 2024, [data set], https://doi.org/10.57746/EO.01jdvcydwjf63vpdbjp0vz6v64.

Kobayashi, S., Kumagai, H., and Kuroiwa, H.: A Proposal of Pulse-Pair Doppler Operation on a Spaceborne Cloud-Profiling Radar in the W Band, Journal of Atmospheric and Oceanic Technology, 19, 1294–1306, https://doi.org/10.1175/1520-0426(2002)019%253C1294:APOPPD%253E2.0.CO;2, 2002.

Kollias, P., Tanelli, S., Battaglia, A., and Tatarevic, A.: Evaluation of EarthCARE Cloud Profiling Radar Doppler Velocity Measurements in Particle Sedimentation Regimes, Journal of Atmospheric and Oceanic Technology, 31, 366–386, https://doi.org/10.1175/JTECH-D-11-00202.1, 2014.

Kollias, P., Puidgomènech Treserras, B., Battaglia, A., Borque, P. C., and Tatarevic, A.: Processing reflectivity and Doppler velocity from EarthCARE's cloud-profiling radar: the C-FMR, C-CD and C-APC products, Atmospheric Measurement Techniques, 16, 1901–1914, https://doi.org/10.5194/amt-16-1901-2023, 2023.

Louf, V., Protat, A., Warren, R. A., Collis, S. M., Wolff, D. B., Raunyiar, S., Jakob, C., and Petersen, W. A.: An Integrated Approach to Weather Radar Calibration and Monitoring Using Ground Clutter and Satellite Comparisons, Journal of Atmospheric and Oceanic Technology, https://doi.org/10.1175/JTECH-D-18-0007.1, 2019.

Louf, V. and Protat, A.: Real-Time Monitoring of Weather Radar Network Calibration and Antenna Pointing, Journal of Atmospheric and Oceanic Technology, https://doi.org/10.1175/JTECH-D-22-0118.1, 2023.

Mitchell, D. L.: Use of Mass- and Area-Dimensional Power Laws for Determining Precipitation Particle Terminal Velocities, Journal of the Atmospheric Sciences, 53, 1710–1723, https://doi.org/10.1175/1520-0469(1996)053%253C1710:UOMAAD%253E2.0.CO;2, 1996.

Nakamura, K. and Furukawa, K.: Estimation of Doppler Velocity Degradation Due to Difference in Beam-Pointing Directions, IEEE Geoscience and Remote Sensing Letters, 20, 1-5, 2023.

National Centers for Environmental Prediction/National Weather Service/NOAA/U S. Department of Commerce: NCEP FNL Operational Model Global Tropospheric Analyses, continuing from July 1999, https://doi.org/10.5065/D6M043C6, 2000.

https://doi.org/10.5194/egusphere-2025-4819
Preprint. Discussion started: 9 October 2025

Puigdomènech Treserras, B., Kollias, P., Battaglia, A., Tanelli, S., and Nakatsuka, H.: EarthCARE’s Cloud Profiling Radar Antenna Pointing Correction using Surface Doppler Measurements, EGUsphere, 1–16, https://doi.org/10.5194/egusphere-2025-1680, 2025.

Radenz, M., Bühl, J., Seifert, P., Baars, H., Engelmann, R., Barja González, B., Mamouri, R.-E., Zamorano, F., and Ansmann, A.: Hemispheric contrasts in ice formation in stratiform mixed-phase clouds: disentangling the role of aerosol and dynamics with ground-based remote sensing, Atmospheric Chemistry and Physics, 21, 17969–17994, https://doi.org/10.5194/acp-21-17969-2021, 2021.

Reverdy, M., Chepfer, H., Donovan, D., Noel, V., Cesana, G., Hoareau, C., Chiriaco, M., and Bastin, S.: An EarthCARE/ATLID simulator to evaluate cloud description in climate models, Journal of Geophysical Research: Atmospheres, 120, 11,090-11,113, https://doi.org/10.1002/2015JD023919, 2015.

Roh, W., Satoh, M., Hagihara, Y., Horie, H., Ohno, Y., and Kubota, T.: An evaluation of microphysics in a numerical model using Doppler velocity measured by ground-based radar for application to the EarthCARE satellite, Atmospheric Measurement Techniques, 17, 3455–3466, https://doi.org/10.5194/amt-17-3455-2024, 2024.

Scarsi, F. E., Battaglia, A., Tridon, F., Martire, P., Dhillon, R., and Illingworth, A.: Mispointing characterization and Doppler velocity correction for the conically scanning WIVERN Doppler radar, Atmospheric Measurement Techniques, 17, 499–514, https://doi.org/10.5194/amt-17-499-2024, 2024.

Seiki, T. and Nagao, T. M.: Evaluation of the Aggregation Efficiency Modeling at Colder Atmospheric Temperatures in Comparison to Satellite Observations, Journal of the Atmospheric Sciences, 81, 1689–1710, https://doi.org/10.1175/JAS-D-23-0208.1, 2024.

Seiki, T., Noda, A. T., Hagihara, Y., and Horie, H.: Dominant Ice Cloud Microphysics Characterized by Simultaneous Observations of Radar Reflectivity and Doppler Velocity, ESSOAr [preprint], https://doi.org/10.22541/essoar.175766898.89999401/v1, submitted to J. Atmos. Sci., 2025.

Torao, M.: On the Deflection of Verticals in Japan, Journal of the Geodetic Society of Japan, 2, 108–110, https://doi.org/10.11366/sokuchi1954.2.108, 1956.

https://doi.org/10.5194/egusphere-2025-4819
Preprint. Discussion started: 9 October 2025

Voors, R., Donovan, D., Acarreta, J., Eisinger, M., Franco, R., Lajas, D., Moyano, R., Pirondini, F., Ramos, J., and Wehr, T.: ECSIM: the simulator framework for EarthCARE, in: Sensors, Systems, and Next-Generation Satellites XI, Sensors, Systems, and Next-Generation Satellites XI, 67441Y, https://doi.org/10.1117/12.737738, 2007.

Warren, R. A., Protat, A., Siems, S. T., Ramsay, H. A., Louf, V., Manton, M. J., and Kane, T. A.: Calibrating Ground-Based Radars against TRMM and GPM, Journal of Atmospheric and Oceanic Technology, https://doi.org/10.1175/JTECH-D-17-0128.1, 2018.

Wehr, T., Kubota, T., Tzeremes, G., Wallace, K., Nakatsuka, H., Ohno, Y., Koopman, R., Rusli, S., Kikuchi, M., Eisinger, M., Tanaka, T., Taga, M., Deghaye, P., Tomita, E., and Bernaerts, D.: The EarthCARE mission – science and system overview, Atmospheric Measurement Techniques, 16, 3581–3608, https://doi.org/10.5194/amt-16-3581-2023, 2023.

Westbrook, C. D., Ball, R. C., Field, P. R., and Heymsfield, A. J.: Theory of growth by differential sedimentation, with application to snowflake formation, Phys. Rev. E, 70, 021403, https://doi.org/10.1103/PhysRevE.70.021403, 2004.

Yamazaki, K. and Miura, H.: On the Formation Mechanism of Cirrus Banding: Radiosonde Observations, Numerical Simulations, and Stability Analyses, Journal of the Atmospheric Sciences, 78, 3477–3502, https://doi.org/10.1175/JAS-D-20-0356.1, 2021.